Mon. Not. R. Astron. Soc. **000**, 000–000 (0000) Printed 4 June 2014 (MN LATEX style file v2.2)

The Hα kinematics of interacting galaxies in 12 compact groups*

S. Torres-Flores[1]†, P. Amram[2], C. Mendes de Oliveira[3], H. Plana[4], C. Balkowski[5], M. Marcelin[2], & D. Olave-Rojas[1]

[1] *Departamento de Física, Universidad de La Serena, Av. Cisternas 1200 Norte, La Serena, Chile*
[2] *Aix-Marseille Université, CNRS, LAM (Laboratoire d'Astrophysique de Marseille), 13388, Marseille, France*
[3] *Departamento de Astronomia, Instituto de Astronomia, Geofísica e Ciências Atmosféricas da USP, São Paulo, Brazil*
[4] *Laboratório de Astrofísica Teórica e Observacional, Universidade Estadual de Santa Cruz, Ilhéus, Brazil*
[5] *GEPI, Observatoire de Paris, Paris University Denis Diderot & CNRS, 5 place Jules Janssen, Meudon, France*

arXiv:1406.0828v1 [astro-ph.GA] 3 Jun 2014

4 June 2014

ABSTRACT

We present new Fabry-Perot observations for a sample of 42 galaxies located in twelve compact groups of galaxies: HCG 1, HCG 14, HCG 25, HCG 44, HCG 53, HCG 57, HCG 61, HCG 69, HCG 93, VV 304, LGG 455 and Arp 314. From the 42 observed galaxies, a total of 26 objects are spiral galaxies, which range from Sa to Im morphological types. The remaining 16 objects are E, S0 and S0a galaxies. Using these observations, we have derived velocity maps, monochromatic and velocity dispersion maps for 24 galaxies, where 18 are spiral, three are S0a, two are S0 and one is an Im galaxy. From the 24 velocity fields obtained, we could derive rotation curves for 15 galaxies; only two of them exhibit rotation curves without any clear signature of interactions. Based on kinematic information, we have evaluated the evolutionary stage of the different groups of the current sample. We identify groups that range from having no Hα emission to displaying an extremely complex kinematics, where their members display strongly perturbed velocity fields and rotation curves. In the case of galaxies with no Hα emission, we suggest that past galaxy interactions removed their gaseous components, thereby quenching their star formation. However, we can not discard that the lack of Hα emission is linked with the detection limit for some of our observations.

Key words: galaxies: evolution – galaxies: interactions – galaxies: kinematics and dynamics

1 INTRODUCTION

Nearby compact groups provide ideal laboratories for studying the effects of ongoing collisions on the structure and dynamics of galaxies. Given their proximity, a detailed study of these systems can help us understand in detail some interaction effects that are common in the distant Universe, where the merger rate was higher than today (e.g. López-Sanjuan et al. 2013).

During the last decade, Hα Fabry-Perot observations of nearby compact groups were used to derive the spatial distribution and kinematics of the warm gas content of galaxies in these systems (e. g. Mendes de Oliveira et al. 1998). The warm gas is a tracer of the potential in a galaxy and a detailed analysis of the kinematics of the emission-line velocity field can be used to determine the influence of the galaxy interactions in the evolution of compact group galaxies, when compared with galaxies in other environments (e. g. using the Tully-Fisher relation, Torres-Flores et al. 2013).

Successive mass accretion marks the history of galaxies in these compact interacting systems. The study of the

* Based on observations made with ESO Telescopes at the La Silla Observatory and the Observatoire de Haute Provence, France. Based on observations obtained at the Gemini Observatory, which is operated by the Association of Universities for Research in Astronomy, Inc., under a cooperative agreement with the NSF on behalf of the Gemini partnership: the National Science Foundation (United States), the Science and Technology Facilities Council (United Kingdom), the National Research Council (Canada), CONICYT (Chile), the Australian Research Council (Australia), Ministério da Ciência e Tecnologia (Brazil) and Ministerio de Ciencia, Tecnología e Innovación Productiva (Argentina) – Observing run: GS-2013B-Q-27.
† E-mail: storres@dfuls.cl

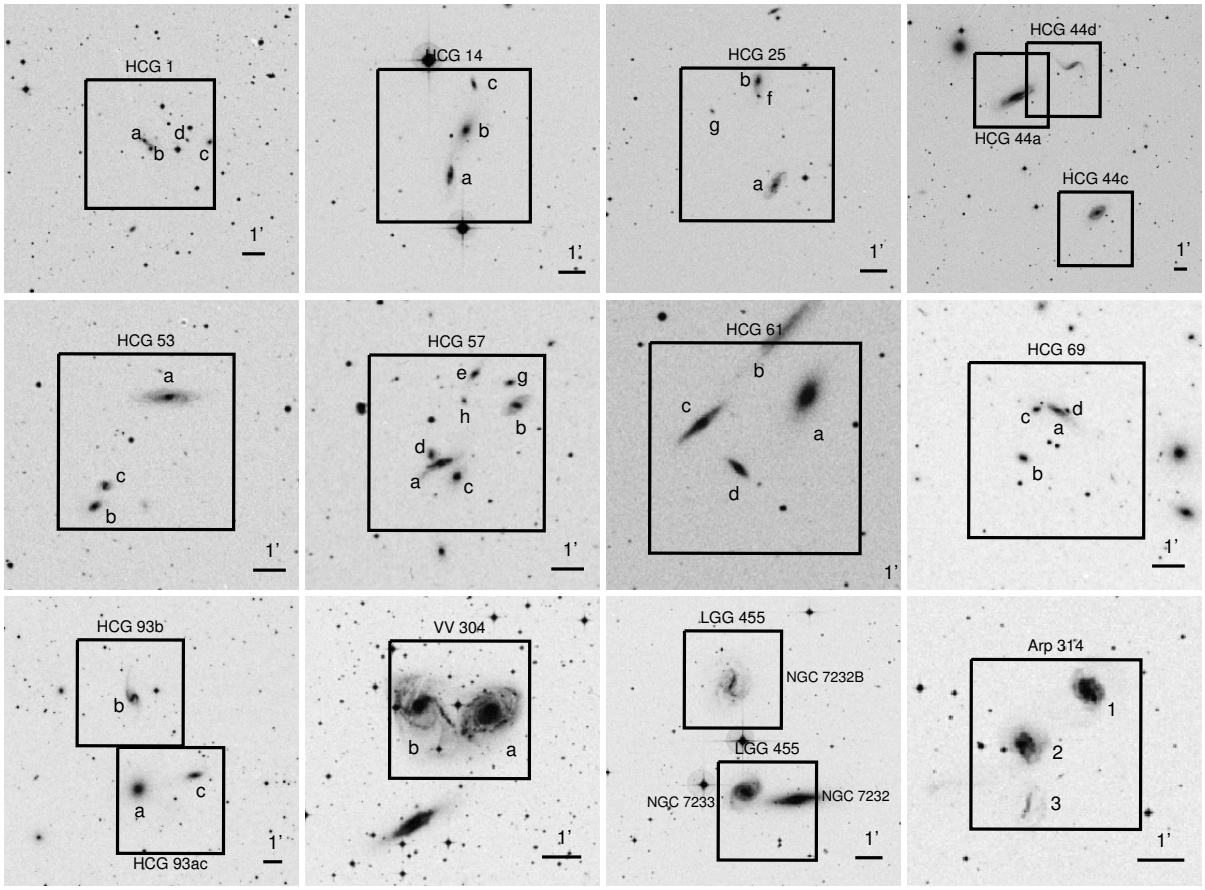

Figure 1. Optical DSS images of the set of twelve compact groups analysed in this paper. In all panels (where North is at the top and East is to the left), black rectangles indicate the field-of-view of the instrument, in which we derived the Hα monochromatic images, velocity fields and dispersion maps by using the Fabry-Perot data cubes. The horizontal line at the bottom right of each panel indicates a scale of 1'.

observed kinematics of a system retains a memory of the accretion process, which drives galaxy evolution. Misaligned stellar and gas major axes position angles, anomalous kinematics structures, complex Hα distribution, distorted spiral arms and disagreement between both sides of the rotation curves are a few of the most common indicators that galaxies have experienced or are experiencing a collision. All of these have previously been identified in compact groups (see Amram et al. 2003 and references in that paper). Also, the formation of tidal tails in compact group galaxies is a typical signature of galaxy-galaxy collision. For example, Renaud et al. (2010) performed N-body simulations of the compact group Stephan' Quintet, recovering on this way the main tails visible in this strongly interacting system.

It is crucial to enlarge the set of interacting and merging candidate galaxies for which we have measured velocity fields in order to shed light on their formation/evolution processes. The present study adds twelve new compact groups (and velocity fields for 24 galaxies) to a total of already 25 groups (with velocity fields derived for 58 galaxies[1]) already published in the last 15 years (Mendes de Oliveira et al. 1998, Plana et al. 2003, Amram et al. 2003, Torres-Flores et al. 2009, 2010, 2013) using Fabry-Perot observations. Besides these works, other kinematical studies of compact groups published during the last decade used HI data (e. g. Verdes-Montenegro et al. 2005, Borthakur et al. 2010). In addition, Nishiura et al. (2000) used longslit observations to analyse the kinematics of HCG galaxies and recently Vogt et al. (2013) used integral field spectroscopy to study the galactic winds in the group HCG 16.

The organization of this article is as follows: Section 2 gives details of the observations and data reduction. In Section 3, we present the results for the internal kinematics and the mass determinations of the individual galaxies of the groups. Section 4 contains the discussion and conclusions.

2 OBSERVATION AND DATA REDUCTION

2.1 The Sample

We have obtained new Fabry-Perot observations for 42 galaxies in twelve small groups: HCG 1, HCG 14, HCG 25, HCG 44, HCG 53, HCG 57, HCG 61, HCG 69, HCG 93, VV 304, LGG 455 and LGG 467. Most of the targets selected here were part of a larger survey study of the kinematics of galaxies in Hickson Compact Groups (e.g. Torres-Flores et al. 2010). To the Hickson sample we have added other three

[1] HCG FabryPerot data are available at http://fabryperot.oamp.fr

systems which are not included in the Hickson (1992) catalogue. These are LGG 455 and LGG 467 (hereafter LGG 467 will be named Arp 314), listed in the catalogue of compact groups of Garcia (1995), and in addition, the well known galaxy triplet VV 304, which is the compact core of a looser group. VV 304 has a median separation between the two brightest galaxies lower than 3 kpc and the centre of the next bright neighbour at the same redshift is about 40 kpc of the centre of the triplet, which makes this system similar to other compact configurations from the Hickson et al. (1992) and Garcia (1995) catalogues. Most of the systems studied here present clear signatures of interactions, making them ideal targets to study the kinematics of the warm ionized gas aiming at studying galaxy evolution in dense environments. All the groups listed above are located in the nearby universe, having radial velocities ranging from 1200 km s^{-1} to ∼10000 km s^{-1}. In Fig. 1 we show a DSS optical image of each target and in Table 1 we list the main properties of each observed galaxy.

2.2 Observations

The observations of HCG 1, 14, 25 and 93 were carried out in October 2012, using the GHASP Fabry-Perot instrument mounted on the 1.93 m telescope at the Observatoire de Haute Provence (OHP). The groups HCG 44, 53, 57, 61 and 69 were observed with the same instrument and observing setup, in April 2011. For HCG 14 we have observed two fields, which cover the members HCG 14a, b and c. For HCG 57 and HCG 69 we have observed two fields, which cover members a, b, c, d, e, g, h and a, b ,c , d, respectively. Systems VV 304, LGG 455 and Arp 314 were observed by using the Fabry-Perot instrument CIGALE mounted on the European Southern Observatory (ESO) 3.6 m telescope at La Silla (Chile) in September 2000.

For the ESO and OHP observations, the interference order of the Fabry-Perot was $p = 793$ at Hα and $p = 798$ at Hα, respectively, where the free spectral range (FSR) was 378 km s^{-1} and 376 km s^{-1} in each case. For both observations we scanned 32 steps, which gave us sampling steps of ∼11.8 km s^{-1} in both cases (R∼12000). The information was recorded by using a photon counting system, where the pixel size was 0.41″ pix^{-1} at ESO and 0.69″ pix^{-1} at OHP. Exposure times of 1.1, 1.6, 1.1 and 0.8 hours were used to observe Arp 314, VV 304, LGG 455ab and LGG 455c, respectively; for the rest of the sample, the total exposure time was 2 hours. In Table 2 we summarize the instrumental setup used in the observations.

2.3 Data Reduction

The Fabry-Perot data were reduced by using the package developed by Daigle et al. (2006). One of the main advantages of this reduction package consists in the use of an adaptive spatial binning, based on the 2D Voronoi tessellation method, applied to the 3D data cubes. Details about data reduction using this package can be found in Epinat et al (2008).

For the data cubes used in this study, an adaptive spatial binning was applied to the data, in order to recover information on regions having low signal-to-noise ratios (SNR). This allows optimizing the spatial resolution to the SNR of the data. The adaptive binning allows reaching an uniform SNR over the whole field-of-view with the highest possible spatial resolution. Indeed, with the spatial adaptive binning technique, a bin is aggregating new pixels until it has reached a given level that is set *a priori*, called the signal-to-noise target (SNRt). For each bin, the noise is determined from the r.m.s of the continuum (the line-free region of the whole spectrum). The SNR is thus the ratio between the flux in the line and the r.m.s. in the continuum. Starting from an initial SNR, a pixel spectrum may be binned with spectra of neighbour pixels to yield a new pixel of larger size (called a bin) and of larger SNR. Disk regions of initial SNR higher than SNRt (e.g. in the inner galaxy regions, spiral arms, star forming regions) are not binned, maintaining the angular resolution as high as possible. On the other hand, the angular resolution in disk regions with initial low SNR (e.g. disk outskirts, interarm regions) is decreased during the binning process in order to obtain an increase in SNR. Results presented here have been obtained with SNRt=5 per bin for HCG compact group. In the case of the compact groups VV 304, LGG 455 and Arp 314 (observed at ESO), we used a SNRt=6, in order to avoid some artefacts present in the data at low SNR.

In order to quantify the mean SNR of a given data cube and its associated set of 2D maps, we have defined the index called SNRi (for signal-to-noise ratio index). It measures, above a certain flux threshold defining the galaxy area, the average number of pixels that need to be binned in order to reach the desired total SNRt. SNRi is thus defined as the total number of pixels divided by the total number of bins. As an example, if the image contains 10,000 pixels and 1,000 bins, SNRi=10 and, on average, 10 pixels are needed to be aggregated to form a bin for a given SNRt. The smaller the value of SNRi, the higher is the mean SNR of that region; SNRi could not be lower than unity given that SNRi=1 means that an individual pixel has a SNR equal or higher than SNRt and no binning is necessary (and in that case the number of bins is equal to the number of pixels).

The OH sky lines were extracted by creating a data cube of the regions where no galaxies were located. Wavelength calibrations were obtained by scanning the Ne 6598.95 Å line under the same conditions as the observations. In the end of the reduction process, we obtained the velocity field, the Hα monochromatic, the continuum and the velocity dispersion map of each galaxy.

Velocity dispersion maps have been corrected from instrumental broadening. In the case of OHP galaxies (see section 2.2), we have used the instrumental dispersion map derived from the Neon calibration lamp. For ESO objects (see section 2.2), due to a lower SNR in the calibration data, we derived a mean instrumental correction over the whole field (which corresponds to σ_{inst}=5.6 km s^{-1}). We note that in the latter case the instrumental broadening does not change more than 10% over the extension of the galaxies. Under the assumption that the observed and instrumental profiles can be fitted with Gaussian functions, the actual velocity dispersion σ can be obtained using $\sigma = \sqrt{\sigma^2_{observed} - \sigma^2_{inst}}$. For a comparison, in Table 3 (column 8) we list the mean velocity dispersion for each galaxy (values that are corrected for σ_{inst}). In the case of the groups HCG 14, 57 and 69, which were observed twice, we have added the data, in order to in-

Table 1. Main properties of the sample

(1) ID	(2) ID (Alternative name)	(3) α (2000) h:m:s	(4) δ (2000) d:m:s	(5) Morph type	(6) T type	(7) V_{syst} km s^{-1}	(8) Distance Mpc	(9) B_{Tc} mag	(10) B-R mag	(11) Seeing Arcsec
HCG 1a	UGC 00248 NED01	00:26:07.14	+25:43:30.2	Sc	7	10237	137.8	14.43	1.29	4.5
HCG 1b	UGC 00248 NED02	00:26:05.99	+25:43:08.2	Im	12	10266	138.2	15.04	1.36	4.5
HCG 1c	...	00:25:54.48	+25:43:24.0	E0	0	10056	135.3	15.57	1.69	4.5
HCG 1d	...	00:25:58.86	+25:43:29.7	S0	1	10120	136.2	16.50	1.60	4.5
HCG 14a	MCG -01-06-022	01:59:49.82	-07:03:32.9	Sb	5	5929	77.9	14.77	1.86	3.6
HCG 14b	MCG -01-06-020	01:59:52.23	-07:05:11.5	E5	0	5365	71.3	14.17	1.54	3.6
HCG 14c	MCG -01-06-019	01:59:48.69	-07:01:50.9	Sbc	6	5145	68.3	16.58	1.94	3.6
HCG 25a	UGC 02690	03:20:43.15	-01:06:33.7	SBc	7	6285	83.6	13.86	1.05	4.4
HCG 25b	UGC 02691 NED01	03:20:45.59	-01:02:41.5	SBa	3	6408	84.2	14.45	1.75	4.4
HCG 25f	UGC 02691 NED02	03:20:45.55	-01:03:15.3	S0	1	6279	83.0	16.98	1.52	4.4
HCG 25g	...	03:20:52.32	-01:03:48.5	S0	1	12179	164.0	16.93	1.70	4.4
HCG 44a	NGC 3190	10:18:06.12	+21:49:52.8	Sa	3	1293	22.6	11.52	1.28	2.3
HCG 44c	NGC 3185	10:17:38.73	+21:41:17.6	SBc	7	1218	21.6	12.55	0.97	2.3
HCG 44d	NGC 3187	10:17:48.00	+21:52:23.9	Sd	9	1579	27.3	13.09	0.26	2.2
HCG 53a	NGC 3697	11:28:50.37	+20:47:43.2	SBbc	6	6261	92.9	12.91	1.30	2.7
HCG 53b	NGC 3697C	11:29:00.00	+20:44:22.0	S0	1	6166	93.9	14.73	1.57	2.7
HCG 53c	NGC 3697B	11:28:58.55	+20:45:00.1	SBd	9	6060	92.7	14.81	1.00	2.7
HCG 57a	NGC 3753	11:37:53.78	+21:58:51.0	Sb	5	8727	126.5	13.99	1.73	5.9
HCG 57b	NGC 3746	11:37:43.68	+22:00:33.6	SBb	5	9022	130.5	14.32	1.55	5.9
HCG 57c	NGC 3750	11:37:51.75	+21:58:25.8	E3	0	9081	131.3	14.63	1.57	5.9
HCG 57d	NGC 3754	11:37:55.12	+21:59:08.3	SBc	7	8977	129.9	14.51	1.26	5.9
HCG 57e	NGC 3748	11:37:49.17	+22:01:32.8	S0a	2	8992	127.7	15.37	1.71	5.9
HCG 57g	NGC 3745	11:37:44.61	+22:01:15.0	SB0	1	9416	136.5	15.84	1.65	5.9
HCG 57h	...	11:37:50.69	+22:00:42.7	SBb	5		133.5	16.75	1.53	5.9
HCG 61a	NGC 4169	12:12:18.55	+29:10:47.3	S0a	2	3784	59.3	12.82	1.50	2.8
HCG 61c	NGC 4175	12:12:30.95	+29:10:06.7	Sbc	6	3956	62.4	13.53	1.56	2.8
HCG 61d	NGC 4174	12:12:26.77	+29:08:56.8	S0	1	3980	62.9	14.12	1.40	2.8
HCG 69a	UGC 08842 NED02	13:55:29.86	+25:04:25.9	Sc	7	8856	129.5	14.94	1.57	2.3
HCG 69b	...	13:55:34.41	+25:02:58.4	SBb	5	8707	127.7	15.59	1.49	2.3
HCG 69c	UGC 08842 NOTES01	13:55:32.62	+25:04:27.4	S0	1	8546	125.3	14.94	1.45	2.3
HCG 69d	UGC 08842 NED01	13:55:28.35	+25:04:24.7	SB0	1	9149	129.6	16.06	1.51	2.3
HCG 93a	NGC 7550	23:15:16.03	+18:57:41.3	E1	0	5140	69.2	12.61	1.60	2.8
HCG 93b	NGC 7549	23:15:17.21	+19:02:29.7	SBd	9	4672	64.8	13.18	1.30	3.6
HCG 93c	NGC 7547	23:15:03.64	+18:58:23.2	SBa	3	5132	65.2	13.94	1.79	2.8
VV 304a	NGC 6769	19:18:22.70	-60:30:04.0	SABb	...	3686	54.0	12.55	...	1.5
VV 304b	NGC 6770	19:18:37.30	-60:29:47.0	Sb	...	3841	56.4	12.83	...	1.5
NGC 7232	...	22:15:38.00	-45:51:00.0	S0a	...	1915	27.3	12.95	...	1.2
NGC 7232B	...	22:15:52.40	-45:46:50.0	SBm	...	2160	30.9	13.9	...	1.3
NGC 7233	...	22:15:49.00	-45:50:47.0	S0a	...	1841	26.3	13.09	...	1.2
Arp 314-1	MCG -01-58-009	22:58:02.20	-03:46:11.0	Sbc	...	3687	51.1	13.70	...	1.1
Arp 314-2	MCG -01-58-010	22:58:07.90	-03:47:20.0	SBc	...	3731	51.7	13.81	...	1.1
Arp 314-3	MCG -01-58-011	22:58:07.30	-03:48:38.0	SBd	...	3701	51.3	16.00	...	1.1

(1) Galaxy ID; (2) Most commonly used name for each galaxy, when available; (3) Right Ascension; (4) Declination; (5) Morphological Type; (6) T-type morphological type; (7) Systemic velocity; (8) Distance in Mpc (corrected for the Virgo, Great Attractor and Shapley supercluster infall. Values were taken from NED); (9) B-band magnitude; (10) Optical (B-R) colors; (11) Seeing (arcsec). In the case of HCG galaxies, all quantities were taken from Hickson 1993, except the Right Ascension and Declination that were taken from the Vizier database and the T-type morphological classification, which was taken from Hickson et al. (1989). For other galaxies, the information was taken from the NED database, except for the morphological types that were taken from the HyperLeda database.

crease the SNR and the different maps were derived from the added Hα data cubes. Given the low-level emission detected for HCG 44a and HCG 61, we have masked the velocity maps by using the monochromatic images.

2.4 Flux calibration

The Fabry-Perot data described above have been obtained mainly to study the kinematic of compact groups galaxies. For this reason, we have taken no data for flux calibrators. However, an indirect calibration of the Fabry-Perot data, taken at taken at ESO, has been made using new Gemini GMOS multislit observations of the system VV 304. These data were observed during the program GS-2013B-Q-27 (PI:

Table 2. Journal of Fabry-Perot observations

Observations	Telescope	ESO 3.6m	OHP 1.93m
	Equipment @ Cassegrain focus	CIGALE	GHASP
	Date	2000, Sept.	2011, April & 2012, October
Spatial sampling	Total Field	207"×207"	353"×353"
	Pixel Size (binned)	0.405"	0.69"
Calibration	Neon Comparison light	λ 6598.95 Å	λ 6598.95 Å
Fabry–Perot	Interference Order	793 @ λ 6562.78 Å	798 @ λ 6562.78 Å
	Free Spectral Range at Hα	378 km s^{-1} (8.28 Å)	376 km s^{-1} (8.22 Å)
	Finesse at Hα	11.4	11.9 (run 2011) –11.0 (run 2012)
	Instrumental FWHM	33 km s^{-1}	32 km s^{-1} (run 2011) – 34 km s^{-1} (run 2012)
	Spectral resolution at Hα	12682	12774
Spectral sampling	Number of Scanning Steps	32	32
	Sampling Step	0.26 Å (11.81 km s^{-1})	0.26 Å (11.75 km s^{-1})
Detector	IPCS	GaAs Tube	GaAs Tube

S. Torres-Flores), with a resolution that enabled us to separate the [NII] lines from the Hα emission. Data reduction was performed using the Gemini Data reduction package in IRAF. In these observations the slit width was set to 1 arc sec, and the length of the slit was changed depending on the size of each source. In order to do the flux calibration, we have used a sample of 18 sources detected in the spiral arms of VV 304, which displayed typical spectra of a HII regions. For each source we have measured the Hα flux by using the task SPLOT in IRAF. In order to compare these Hα fluxes (erg s^{-1} cm^{-2}) with the Hα emission coming from the Fabry-Perot data (counts per seconds), we have used the monochromatic map produced in the data reduction process. In that map, we measured the Hα emission in the same extraction windows that were defined in the multislit data reduction. The result of this analysis is shown in Figure 2, where we adjusted a linear fit to the data. In this case we have set the zero point equal to zero. The resulting fit gave us a coefficient (slope) of 3.39×10^{-18} erg s^{-1} cm^{-2} counts^{-1} s. Finally, this value was used to calibrate the Fabry-Perot monochromatic maps of VV 304, LGG 455 and Arp 314, assuming that LGG 455 and Arp 314 were observed under the same conditions as VV 304 (which was the case - the nights were photometric in all cases, and they were taken in subsequent nights, with the same instrumentation. In the case of compact groups observed at OHP we have attempted to do a flux calibration using the Hα maps published by Vilchez et al. (1998), however these images do not provide a lower limit for the shown flux. Therefore, it was not possible to use these data as calibrators.

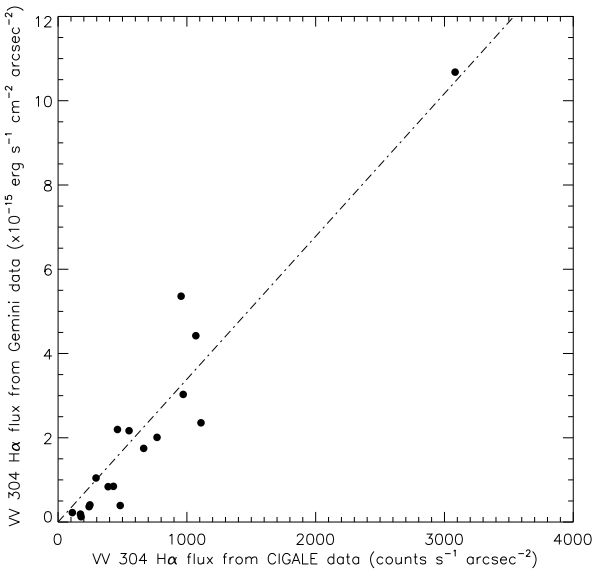

Figure 2. Comparison between the Hα fluxes measured from the monochromatic Fabry-Perot maps versus the Hα fluxes derived from the Gemini/GMOS multislit observations of VV 304. The dashed-dotted line shows a linear regression on the data, where the zero point has been fixed to zero.

2.5 Kinematic parameters and rotation curves

For each galaxy, the kinematic position angle, inclination and systemic velocity and rotation curve were estimated by fitting a modeled velocity field to the observed data and minimizing the residual velocity dispersion, following the method described in Epinat et al. (2008). Due to the fact that the velocity fields of these perturbed systems are complex, the centre of the models were not left free but fixed by using the morphological centre of the galaxies defined as the peak of the continuum image (as done by Torres-Flores et al. 2010). This procedure allowed us to reduce the number of free parameters in the computation of the rotation curves of the galaxies. We note that some groups have been observed under poor seeing conditions. This fact is not a problem in the case of the velocity fields that we derived, given that each bin corresponds to a given signal-to-noise ratio independently of the size of the seeing disk. Also, the rotation curves were plotted taking into account the seeing value (see Epinat et al. 2008).

For 27 galaxies out of the 42 in our sample, it was not possible to derive a rotation curve, mainly for two reasons: (1) a few galaxies do not show enough Hα emission, (2) a few galaxies have a velocity field that is too perturbed; in both cases it is impossible to obtain the rotation curve based on the warm ionized gas component. Due to the fact that they are not dominated by circular motions, perturbed velocity maps can not be modeled in a reliable way, they produce unrealistic estimations for the kinematic inclinations and position angles of the major axis of the galaxy. On the

other hand, less perturbed velocity fields need nevertheless specific treatment. This is the case for velocity fields for which the kinematic position angle is affected by a strong bar that dominates most of the emission within the optical disk (e.g. HCG 44d). In such cases, it is necessary to fix the position angle of the major axis by using the morphological value determined outside of the bar. In other cases the computation of the kinematic inclination yielded a value close to that for an unrealistic face-on galaxy (e.g. HCG 1ab, HCG 53c and VV 304b). In those cases, we have to fix the inclination of the galaxy by using its morphological value (e.g. $i_{morph} = 44$ degrees for HCG 1ab, $i_{morph} = 52$ degrees for HCG 53c and $i_{morph} = 46$ degrees for VV 304b). We also had to fix the inclination by using the morphological value for galaxies having a too irregular morphology which makes it difficult to get a kinematic measurement (e.g. NGC 7232B). In Table 3 we list the main kinematic parameters for the galaxies for which we measure Hα emission, together with their respective morphological parameters (i.e. position angles and inclinations). In the same Table we include late-type spiral galaxies for which we do not detect Hα emission. We note that in several cases it was not possible to derive the kinematic parameters (as discussed above), however, we have included these objects in Table 3 in order to show their SNRi estimations.

In order to quantify the disagreement between both sides of the rotation curves, we have estimated the mean velocity difference for each curve. In most of the cases both sides of the rotation curves do not reach the same radius. In addition, the sampling of both sides is not the same (given the variations in the Hα emission across of the galaxy). For these reasons, we have quantified the disagreement between both sides only up to the last radius for the less-extended side of the rotation curve, where we have matched the spatial sampling of both sides. In Table 3 we list the asymmetries in the rotation curve for each galaxy. In this table we have also included the maximum rotational velocity for each galaxy, which was obtained from the rotation curves. This rotational velocity was used to obtain the dynamical mass for each galaxy, which was estimated by assuming that the mass has a spherical distribution. We have computed the dynamical mass of each galaxy at their optical radius and also at the last observed point in the rotation curve (in the more-extended side of the curve). These values are listed in Table 4.

3 KINEMATIC DESCRIPTION OF EACH INTERACTING SYSTEM

In this section we describe the main kinematic features for the members of the studied groups. In Appendix A (online data only, Figs. A1 to A14) we show, for each observed field, an optical DSS image (top left), a velocity field (top right), an Hα monochromatic image (bottom left) and a dispersion map (bottom right). In Appendix B (online data only, Fig. B1) we show a rotation curve for each galaxy, when it was possible to derive it. As an example, in Fig. A11 (included in the electronic version of this paper) we shown the different maps that we derived for the members of the system VV 304, and in Figure B1 (also included in the electronic version) we shown the rotation curves that we derived for galaxies VV 304a and VV 304b. The distances to the groups were taken from NED. Distances were corrected for the Virgo, Great Attractor and Shapley supercluster infall (Mould et al. 2000).

3.1 HCG 1

Fig. A1 shows the various maps obtained for HCG 1a and 1b. The Hα map of HCG 1 reveals a diffuse Hα emission for these two galaxies, although they are respectively of Sc and Im type. The galaxies HCG 1c and 1d do not have any Hα emission, which is consistent with their morphological types (E0 and S0, respectively). One should note that the transmission of the interference filter we used was quite low ($\sim$40%). Interestingly, the Hα emission shown in Fig. A1 is mainly concentrated in the bridge connecting HCG 1a and HCG 1b, also detected in the optical images of this system (see Hickson 1993). Since the 3D shape of the group is not known, it is not possible to tell if material is flowing along this bridge. Despite the irregular Hα morphology of this system, a velocity field was derived. The rotation curve derived from this map (see Fig. B1) shows a disagreement in the inner part, however, in the outer part both sides match. In this case, we measure an asymmetry of 28 km s^{-1}.

3.2 HCG 14

No Hα emission was detected in this group, despite a long exposure time and the relatively late morphological types of two of its galaxies. However, as for HCG 1cd, we note that the transmission of the interference filter we used was quite low (in this case $\sim$25%).

3.3 HCG 25

We observed four members of the group (HCG 25a, b, f and g) in the same field of view but detected Hα emission only for HCG 25a.

The Hα emission map (Fig. A2) suggests that the northern side of the galaxy is forming stars more actively than the southern side, with a prominent northern spiral arm. However the brightest star forming region is located on the southern side. The velocity field shown in Fig. A2 is fairly regular, in agreement with the general morphology of this galaxy. The velocity dispersion map shows a mean value of σ=26 km s^{-1}.

The rotation curve of HCG 25a, shown in Fig. B1, reaches values of $\sim$180 km s^{-1}. Despite the regular grand design of its velocity field, the rotation curve of this galaxy shows some differences between the approaching and receding sides. On average, this disagreement reaches a value of 23 km s^{-1}. Nevertheless, the rotation curve increases for both sides out to the optical radius of the galaxy, where it reaches a maximum. A small offset of the kinematical centre (2 arcsec, i.e. 0.8 kpc, to the North-West) could reconcile the two sides of the rotation curve in their rising part, then resulting in a velocity difference of about 30 km s^{-1} between the two sides of the curve in the outer parts. Considering the high inclination of the galaxy (65 degrees) this apparent offset could be due to dust extinction.

Table 3. Kinematic properties of the sample. In this table we have included all the galaxies for which we expect Hα emission following their morphological types.

(1) Galaxy	(2) PA_{kin} deg	(3) PA_{morph} deg	(4) i_{kin} deg	(5) i_{morph} deg	(6) V_{sysFP} km s^{-1}	(7) V_{max} km s^{-1}	(8) Asymmetry km s^{-1}	(9) Mean σ km s^{-1}	(10) SNRi
HCG 1ab	43	50	10*	44	10001±6	344±76	28	25	19.1
HCG 14a	...		...		...	...	...	*nd*	*nd*
HCG 14c	...		...		...	...	...	*nd*	*nd*
HCG 25a	146±2	147	65±3	63	6231±2	170±9	23	26	4.2
HCG 44a	...		...		...	...	...	*nd*	20.1
HCG 44c	137±1	131	53±3	54	1228±2	163±11	8	20	16.6
HCG 44d	...		...		...	...	...	25	8.5
HCG 53a	92±1	93	72±1	70	6206±1	266±8	13	24	11.1
HCG 53c	104±4	122	52*	52	6183±2	69±21	6	26	7.3
HCG 57a	...		...		...	...	...	*nd*	*nd*
HCG 57b	...		...		...	...	...	*nd*	*nd*
HCG 57d	28±2	25	61±8	26	8857±3	121±12	9	26	4.2
HCG 61c	...		...		...	...	...	*nd*	20.1
HCG 69a	...		...		...	...	...	24	15.4
HCG 69b	...		...		...	...	...	*nd*	*nd*
HCG 93b	155±4	39	29±18	70	4676±7	364±203	45	23	10.4
HCG 93c	...		...		...	...	...	*nd*	*nd*
VV 304a	104±2	120	39±12	42	3811±3	245±66	20	27	4.9
VV 304b	58±5	33	46*	46	3867±7	207±79	70	25	6.9
NGC 7232	108±2	100	64±7	86	1810±3	194±14	27	26	12.5
NGC 7232B	162±8	1	32*	32	1775±2	68±48	27	28	20.1
NGC 7233	14±2	...	85±4	29	1848±8	85±8	8	51	1.0
Arp 314-1	115±2	33	18±14	48	4042±1	159±116	26	27	4.9
Arp 314-2	70±6	...	75±23	22	4031±7	210±24	32	30	4.9
Arp 314-3	130±4	175	70±18	90	3757±2	94±12	10	25	15.0

(1) Galaxy ID; (2) Position angle deduced from the velocity field derived in this work; (3) Optical position angle taken from HyperLeda. The position angle is the position angle of the major axis of the 25 mag arcsec^{-2} isophote, in the B-band. In the case of HCG 57d, no position angle estimation was found and we estimated it by visual inspection of the optical image; (4) Inclination deduced from the analysis of the velocity field derived in this work. An asterisk indicates a case when we fixed the inclination by using the morphological value (column 5); (5) Morphological inclination taken from HyperLeda. In the case of the HCG galaxies, this value was taken from the axial ratio (cos(b/a)=i); (6) Systemic velocity deduced from the velocity field analysis; (7) Maximum rotational velocity derived from the rotation curve; (8) Disagreement (asymmetry) between both sides of the rotation curve; (9) Mean velocity dispersion (σ) in the whole field of the galaxy, corrected for instrumental width. In cases where the level of Hα emission is low (as confirmed by the SNRi), we list the σ value as *nd* (no detection). In the case of HCG 1a and 1b, we list the mean velocity dispersion of the Hα emission detected in the bridge between them: (10) SNRi index. It measures the averaged number of pixels per bin thus indicates the mean signal-to-noise ratio in the 2D maps (see section 2.3): lower is this value, higher is the mean SNR, it is quality index. In cases where we do not detect Hα emission, we list the SNRi value as *nd* (no detection).

3.4 HCG 44

Three different fields have been observed for HCG 44, covering members HCG 44a, c and d respectively. The galaxy HCG 44a shows little Hα emission in the centre and in two blobs (at a very low level) as can be seen in Fig. A3. No velocity field can be obtained from our data. HCG 44c shows Hα emission distributed along a ring (Fig. A4) with a strong peak at the centre of the galaxy (as expected for a Seyfert 2 galaxy) and a brighter emission on both ends of the major axis. This Hα annular emission coincides with the UV *GALEX* emission of this galaxy (see Gil de Paz et al. 2007). The ring seen in our Hα image could be the result of the overlaping of two tight spiral arms of this galaxy. Its velocity field is quite regular, with no signatures of any interaction. The position angle of the kinematical major axis is well defined, together with the isovelocity lines across its main body. The rotation curve of this object reflects its ring-like structure, as can be seen in Fig. B1. In the inner first kpc, the rotation curve increases strongly, almost linearly. Between 1 and 2 kpc there is no information, given the lack of Hα emission there. From 2 to 4 kpc the curve keeps increasing gently, reaching a maximum value of about 160 km s^{-1}, close to the optical radius, with a very good agreement between approaching and receding sides of the galaxy, which produces a mean asymmetry of 8 km s^{-1} between both sides.

The Hα emission map of HCG 44d shows several strong emitting knots along a bar-like structure. Strangely, this galaxy was not classified as barred by Hickson (1993) although the B and R-band images (from the Hickson's catalogue and available in the NED database) show a prominent bar. The two arms starting at the end of the bar are exceedingly open, suggesting that their origin could be linked to a past or ongoing tidal interaction. Two emitting sources are conspicuous in the northeastern spiral arm whereas only diffuse Hα emission can be seen in the southwestern arm (Fig.

Table 4. Dynamical masses for the galaxies of this sample

(1) Galaxy	(2) R_{max} kpc	(3) R_{25} kpc	(4) V_{max} km s^{-1}	(5) Mass at R_{max} $\times10^{10}$ M$_\odot$	(6) Mass at R_{25} $\times10^{10}$ M$_\odot$
HCG 25a	18.13	15.81	170±9	12.0	11.0
HCG 44c	5.82	6.786	163±11	3.6	4.2
HCG 53a	32.93	30.81	266±8	54.0	51.0
HCG 53c	5.87	9.438	69±21	0.6	1.0
HCG 57d	14.5	7.557	121±12	4.9	2.6
HCG 93b	22.28	26.39	364±203	68.0	81.0
VV 304a	16.75	18.06	245±66	23.0	25.0
VV 304b	17.6	18.87	207±79	18.0	19.0
NGC 7232	8.02	10.32	194±14	7.0	9.0
NGC 7232B	6.34	7.64	68±48	0.7	0.8
NGC 7233	1.81	6.503	85±8	0.3	1.1
Arp 314-1	6.58	8.175	159±116	3.9	4.8
Arp 314-2	10.73	9.775	210±24	11.0	10.0
Arp 314-3	11.7	8.207	94±12	2.4	1.7

(1) Galaxy ID; (2) Maximum radius reached by the rotation curve; (3) Optical radius of the galaxy; (4) Maximum rotational velocity for each galaxy; (5) Dynamical mass estimated at R_{max}; (6) Dynamical mass estimated at R_{25};

A5). The velocity field of HCG 44d is dominated by the bar. The isovelocities are almost parallel to the bar. The velocity amplitude along the kinematical major axis reaches a value of ∼160 km s^{-1}. The velocity dispersion map reaches its highest values all over the bar, ranging from $\sigma_{observed}$ ∼25 to 40 km s^{-1}. Because of the strong bar and the tidal arms, it was not possible to draw a reliable rotation curve for this galaxy, although we fixed the position angle by using its morphological value.

3.5 HCG 53

Our Fabry-Perot data cover galaxies HCG 53a, 53b and 53c but Hα emission was found only in a and c.

The monochromatic emission distribution in HCG 53a reaches the optical radius of the galaxy. It is asymmetric (see Fig. A6) with bright Hα emission regions on the eastern side. Interestingly, the *GALEX* data of this galaxy show an homogeneous emission across the whole galaxy. Note also that HCG 53 was not detected in the infrared by Allam et al. (1996). The velocity field has been derived with good quality across the whole galaxy (see Fig. A6). It is regular on the eastern side and slightly warped towards the north, on the western side. The velocity amplitude is roughly ±260 km s^{-1}. There is an excellent agreement between the optical and the kinematical position angles. The rotation curve of HCG 53a is quite regular (see Fig. B1) with a good agreement between the approaching and receding sides and it is almost flat, although very slightly increasing beyond 5 kpc.

The small galaxy HCG 53c has a strong bar, which is clearly seen on the DSS image and on the R-band image of the Hickson's catalogue. Along this structure we detected several bright knots containing almost half of the total Hα emission of the galaxy (see Fig. A6). The brightest Hα emission comes from the south end of the bar. However, no Hα knot is observed on the north end of the bar, which could mean that the star-formation is not linked to a resonance. Another Hα emitting knot coincides with the centre of the galaxy. The bar and the kinematic minor axis position angles have an angular separation of 48 degrees (157 and 25 degrees, respectively) leading to a velocity gradient along the bar of ∼50 km s^{-1} and the strong S shape of the bar signature can be seen in the velocity field. The velocity amplitude along the major axis of the galaxy is ∼90 km s^{-1}. HCG 53c has an increasing rotation curve (Fig. B1) reaching ∼70 km s^{-1} at 6 kpc radius. For this object, we adopted the inclination value suggested by its morphology (52 degrees).

The velocity dispersion is quite homogeneous across the whole disk of both HCG 53a and 53c, with values of σ=24 and 26 km s^{-1} respectively.

3.6 HCG 57

Galaxies HCG 57a, b, c, d, e, g and h were observed in the same field of view (member f was about 1' outside the field). Two observations were made, on two successive nights, with different interference filters. The first observation, with rather bad seeing, was made through a filter centred at 673.5 nm (FWHM 1.0 nm) best suited for components 57b, c, d and e. The second observation, with good seeing, was made through a filter centred at 672 nm (FWHM 1.0nm) better suited for HCG 57a but does not show any clear Hα emission despite these good conditions. Only member d displays strong Hα emission all over its disk (see Fig. A7) even through the worse-suited filter was used. No Hα emission could be seen for HCG 57c, e, g and h and there is but a suspicion of faint emission on both sides of HCG 57b (northwest and southeast), possibly coming from the spiral arms. Also *GALEX* data clearly show UV emission for member d only and some diffuse *GALEX* UV emission can be seen for member b.

HCG 57 has been observed in mid-IR by Bitsakis et al. (2010) showing that galaxy d has, by far, the highest SFR of the group, which is consistent with our Hα observation.

The Spitzer IR spectrum of HCG 57a suggests a non-star-forming mechanism able to excite the H2 in the disk of the galaxy, showing that this group may be in a specific phase of rapid transformation (Cluver et al. 2013). HCG 57a is classified as an AGN by Martinez et al. (2010) and as a LINER (low-ionization nuclear emission-line region galaxies) by Gavazzi et al. (2011). HCG 57d is classified as a low-luminosity AGN that coexists with circumnuclear star formation by Martinez et al. (2010).

The Hα emission is strong along the two main spiral arms of HCG 57d, the brightest being the southern arm, which is in the direction of HCG 57a. Almost no Hα emission can be seen in the centre of this galaxy. A diffuse Hα structure extends along the southern spiral arm, connecting HCG 57d with the central region of HCG 57a. We note that the spectrum of 57c and 57g analysed by Martinez et al. (2010) do not show the presence of the Hα emission line, which is consistent with our results. On the other hand, Martinez et al. (2010) found Hα emission for members HCG 57b, 57e and 57h, for which we have detected no emission. This fact may be linked with the detection limit of our current observations.

The velocity field of HCG 57d is fairly regular, with an amplitude of ∼200 km s^{-1} and no clear signature of interaction can be seen despite the apparent proximity of the distorted galaxy HCG 57a. However, there is a small change in the position angle of the major axis along the radius (see Fig. A7). Also, the velocity field is influenced by the Hα extension that seems to connect HCG 57d with the central region of HCG 57a. Finally, the rotation curve of HCG 57d shows a good agreement between the approaching and receding sides up to 6kpc from the centre but both sides do not match in the outer parts. It reaches a maximum velocity of ∼120 km s^{-1} and can be traced beyond the optical radius, where it becomes flat.

The highest values of velocity dispersion are reached along the spiral arms of HCG 57d, following the same ring-like structure (see Fig. A7). The mean value for the whole velocity dispersion map is σ=26 km s^{-1}.

3.7 HCG 61

This group, also known as "The Box", is a triplet formed by HCG 61a, c and d. Allam et al. (1996) confirm the presence of dust and infrared emission in HCG61c. Some Hα emission can be seen in the southeastern side of HCG61 c, corresponding to the brightest region in the B and R-band optical images (see Fig. A8). HCG 61a and d are S0 galaxies for which no Hα emission is expected. However, the central regions of both galaxies display some weak Hα emission, in agreement with the Hα maps from Vilchez et al. (1998). Due to the low SNR of the Hα emission, no rotation curve could be computed for any member of this group.

3.8 HCG 69

HCG 69 is a quartet composed of two late-type galaxies and two lenticulars. HCG 69a shows a strong dust lane across its major axis.

For this group, we have observed twice the same field of view, covering the four members of this system and the two data cubes were added. Very faint Hα emission can be seen for member a, fainter still along the dust lane, as expected (see Fig. A9), whereas no emission at all was found for members b, c and d. *GALEX* ultraviolet emission is bluer for HCG 69a than for HCG 69b and no UV emission is detected for HCG 69c and 69d, as expected from their types. Because of the low SNR of the Hα emission, no rotation curve could be computed for any galaxy of this group.

3.9 HCG 93

Two fields were observed for this group, one for HCG 93a and c and the other one for HCG 93b. No Hα emission has been found for HCG 93a and 93c, as expected from their morphological types. We note that the transmission of the interference filter that we have used was low, close to a ∼25%. Mendes de Oliveira et al. (1994) mention a stellar extension of HCG 93c towards 93a, suggesting a past interaction.

Despite the low transmission of the interference filter, we detected Hα emission in the late-type galaxy HCG 93b (consistent with Torres-Flores et al. 2010), with bright regions on the tips of the bar and on the inner region of the western spiral arm (see Fig. A10). However, the velocity field of HCG 93b is so perturbed, with a strong change of the position angle along the major axis, that we could not compute any rotation curve, even when fixing the kinematical parameters by using their morphological parameters. The stretching of the spiral arms and the perturbation of the velocity field, which cannot be explained by the presence of a strong bar alone, suggest that HCG 93b is interacting with the other galaxies of the group.

3.10 VV 304

VV 304 is a close pair of galaxies inside a quartet (Vorontsov-Velyaminov 1959). VV 304a and VV 304b exhibit perturbed spiral arms on the DSS optical image. For both galaxies, we detect diffuse Hα emission in a ring-like structure on which bright HII regions are superimposed (see Fig. A11; Fig. A11 in Appendix A). Almost no Hα emission is detected in the nuclei of these galaxies where the optical DSS images display strong emission. Both monochromatic images are much alike (see Fig. A11) but VV 304b is a bit brighter. One can see some bright Hα knots in the centre of the pair, where the disks seem to overlap, which could be the result of the interaction.

Despite the interaction, the velocity field of VV 304a looks fairly regular. However, some asymmetries in the isovelocity lines can be seen along the minor axis. Also, this galaxy has a peculiar rotation curve (see Fig. B1). Although the agreement is satisfying between the approaching and receding sides, several bumps can be seen on both sides of the rotation curve. Despite these bumps, the curve remains fairly flat out to 15 kpc, where no more Hα emission is detected (note that the approaching side is more extended because of the overlapping of the disk of VV 304b on the receding side of VV 304a). The velocity dispersion map of VV 304a is rather smooth, without any peak, and displays a mean value of σ= 27 km s^{-1}.

The velocity field of VV 304b is clearly more perturbed

than that of VV 304a, with a difference of almost 30 degrees between the optical and kinematical position angle of the major axis for this galaxy. The southwestern part of the disk (in the direction of VV 304a) displays almost constant radial velocities (about 300 km s^{-1} lower than the velocities of the near side of VV 304a) whereas there is a regular velocity gradient along the major axis on the receding side. As a result, the rotation curve of VV 304b is completely asymmetric (see Fig. B1) confirming the interaction. The velocity dispersion map for this object is similar to that of VV 304a.

3.11 LGG 455

Following Garcia's (1993) catalogue, this group is formed by three spiral galaxies, NGC 7232, NGC 7232B and NGC 7233, and one lenticular galaxy, IC 5181. Subsequently, Garcia (1995) catalogued this group as a compact group.

Two different fields of view where observed for this group, one for NGC 7232 and NGC 7233, the other one for NGC 7232B. The results are given in Fig. A12 and Fig. A13 respectively.

The Hα map of NGC 7232 shows faint diffuse emission all over the disk, with two bright knots, one is close to the nucleus (7.5$''$ west) and the second one is at 22$''$ west from the centre of NGC 7232. A faint tail-like structure can be seen eastward of NGC 7232. The velocity field of NGC 7232 shows a clear velocity gradient along the kinematical major axis, well aligned with the morphological one of the galaxy. The large bin sizes displayed in the velocity field of this galaxy are due to the low SNR of the Hα emission. It results in a patchy appearance of the velocity field, however no strong signature of interaction can be seen. The velocity dispersion map of this galaxy shows the highest values where the monochromatic map peaks, at $\sim$50 km s^{-1}. Despite the fairly regular velocity field of this galaxy, its rotation curve is quite chaotic (see Fig. B1). In the inner part, there is no agreement between both sides of the rotation curve. The approaching side displays a large bump at 10$''$ before growing linearly, whereas the receding side exhibits a large velocity scatter with increasing radius. Furthermore, the rotation curve hardly reaches half the optical radius.

NGC 7233 shows a strong nuclear Hα emission and a faint diffuse Hα emission across the whole optical disk, but no Hα knot on the disk, not even in the spiral arms visible on the optical DSS images. The velocity field shown in Fig. A12 has been masked and limited to the very central part of the galaxy because of parasitic ghost images in the outer parts (the velocity gradient was inverted at large radii, reminding of a problem encountered with HCG 2b by Torres-Flores et al. 2009). As a result, the rotation curve shown in Fig. B1 is limited to the rising part.

Most of the Hα emission of NGC 7232B can be seen in the bar and the departure of the southern spiral arm of this galaxy. The velocity field of NGC 7232B displays a small velocity amplitude $\sim$80 km s^{-1}. The rotation curve of this galaxy (shown in Fig. B1) grows almost linearly with the radius. In the first 10$''$ the velocities display a large scatter, with poor agreement between the approaching and receding sides. The latter climbs at a rotation velocity of 70 km s^{-1}, almost reaching the optical radius.

3.12 Arp 314

Arp 314 is formed by three late-type spiral galaxies: Arp 314 NED01, NED02 and NED03 (hereafter Arp 314-1, Arp 314-2 and Arp 314-3). Garcia (1995) classified this triplet as a compact group (LGG 467). *GALEX* UV images reveal a prominent tidal tail eastward from Arp314-2 and Arp314-3 (Gil de Paz et al. 2007). The *GALEX* UV tidal tail can be seen on optical images such as the Palomar image given in NED or the *SDSS* DR8 release, also showing an outer shell around Arp 314-1, which is another clear signature of interaction. Interestingly, this tidal tail points toward a seemingly fourth small galaxy at about 4 arcmin to the east of Arp 314-3 (however no redshift for this object can be found in the literature).

Our Hα map of Arp 314-1 shows a complex shape (see Fig. A14). The most conspicuous structure is a chain of bright HII regions in the centre, apparently along a spiral arm. These regions exhibit large asymmetric Hα profiles, with a mean width of $\sim$35 km s^{-1} (σ). The brightest Hα emitting region is located at the southwest end of this chain, it is also prominent on the *GALEX* UV images and optical *SDSS* images. The Hα profiles in this bright region are fairly symmetric whereas those observed close to the nucleus are more irregular, with a second component that can be seen on their redshifted side, but it is not detected across the whole disk of the galaxy. Despite the complex Hα morphology of Arp 314-1, its velocity field is fairy regular, with a clear velocity gradient along the kinematic major axis. However some regions show up with abnormal velocities, on both sides of the galaxy and more especially on the southern edge of the disk. Also, we find a strong misalignment between the position angle of the morphological major axis (33 degrees from the Hyperleda database) and the PA of the kinematical major axis (115 degrees from our veocity field). This discrepancy is a clear signature of interaction between galaxies (Torres-Flores et al. 2010). In Fig. B1 we show the rotation curve of Arp 314-1. In the inner 10$''$ we find a strong bump on the receding side, with rotation velocities climbing above 250 km s^{-1}. Then both sides display a slower rotation velocity around $\sim$150 km s^{-1}. Despite the clear signatures of interaction shown by Arp 314-1, its rotation curve remains fairly flat in the outer parts, with a good agreement between both sides.

Arp 314-2 also shows a complex Hα morphology, with most of the Hα emission in the nuclear region and no clear spiral arms. The general pattern is alike that of the *GALEX* UV images and optical *SDSS* images of this galaxy. The Hα profiles observed in the central region are more symmetric than for Arp 314-1, with a σ of $\sim$40 km s^{-1}. The other bright Hα knots found in the disc of this object exhibit symmetric Hα profiles (with an average σ=30 km s^{-1}). Contrary to Arp 314-1 no secondary component is observed on any of the profiles in Arp 314-2. The very central region of Arp 314-2 (inside the first 7$''$ diameter) displays a normal velocity gradient, with no signature of interaction. Outside these first few arc seconds, the velocity field is much more perturbed and chaotic. On the western edge of the disk, one can see a large region with abnormally high velocity. This feature causes a bump on the approaching side of the rotation curve (at $\sim$1 kpc), as shown in Fig. B1. This rotation curve shows a short extension for the receding side ($\sim$4 kpc) whereas the

approaching side reaches a radius of ∼12 kpc, beyond the optical radius. Both sides disagree strongly within the first (∼4 kpc), with quite opposite behaviours. The outer part of the rotation curve is drawn by the approaching side alone, displaying a solid-body shape.

Arp 314-3 looks like an irregular galaxy or alternatively it could be a tidal debris. A few low-intensity Hα emitting regions are detected in the body of this object. These regions have well defined and symmetric Hα profiles. The velocity field shows an amplitude of about 120 km s^{-1} and the resulting rotation curve (see Fig. B1) has a symmetric behaviour for both approaching and receding sides. It rapidly reaches an intermediate flat part with velocities around 40 km s^{-1} at the optical radius (4 kpc) then climbs almost linearly up to 120 km s^{-1} at a radius of 12 kpc. The outer part of the rotation curve must be taken with care however since it has been drawn assuming that Arp 314-3 is a rotating disk whereas the velocity field displays isovelocity lines quite different from those expected with pure circular motions. For instance, one can see unexpectedly high changes in radial velocities along the minor axis, suggesting streaming motions. Also, a strong warp of the disk could explain the apparently high rotation velocities reached by the outermost parts of the rotation curve. Deep red or near infrared band images could help understanding if Arp 314-3 is actually a star forming galaxy containing nevertheless an old stellar population or, alternatively, a recent tidal debris.

4 DISCUSSION AND CONCLUDING REMARKS

Kinematic information on interacting galaxies has been quite useful in the determination of the evolutionary stages of compact groups. Mendes de Oliveira et al. (1998), Amram et al. (2003), Plana et al. (2003) and Torres-Flores et al. (2010) have listed a set of kinematic interaction indicators, which may give insights to the interaction history of galaxies, and hence to the evolutionary stages of the groups to which they belong. For example, Amram et al. (2003) suggested that highly disturbed velocity fields, double nuclei, double kinematic gas components and high amplitude discrepancies between both sides of the rotation curves imply strong galaxy-galaxy interactions or mergers. On the other hand, stellar and gaseous major axes misalignments and tidal tails suggest collisions that may not always lead to merging. Here, we used these indicators to determine the evolutionary stages of the different groups analysed in this paper. In Table 5 we listed the different indicators for each galaxy and in the following we discuss the results for each group.

In **HCG 1**, we detect Hα emission in the bridge between 1a and 1b and a diffuse emission in the centres of members a and b, which suggests that a strong interaction event has occurred in this system. In Stephan's quintet, a group that is widely recognised as being in an advanced stage of evolution, ionized gas is not present in the centres of the member galaxies. In this sense HCG 1 resembles the Stephan's quintet. We conclude that the star formation in the bridge between HCG 1a and 1b may have been strongly enhanced due to interactions.

The three observed galaxies in **HCG 14** (members a, b and c) have morphological types Sb, E5 and Sbc respectively. Despite two of them being spiral galaxies, we do not detect any Hα emission for the member galaxies of this group. The elliptical galaxy HCG 14b was pointed out by Mendes de Oliveira and Hickson (1994, their Fig. 4) to have a surface brightness profile which is shallower than those of other elliptical galaxies of similar luminosities, resembling a surface brightness profile of a cD galaxy (although HCG 14b is an intermediate-luminosity galaxy). This shallow profile may indicate previous merging events. We suspect that this group could be the result of one or more past mergers or accretion events, given the shallow profile of HCG 14b, but this question remains open, awaiting further observations

We observed three galaxies in **HCG 25**, members a, b and f. There are four other galaxies (c, d, e and g) originally catalogued by Hickson (1982) to be members of the same group but which are actually part of another system in the foreground. Only for HCG 25a (an SBc galaxy) we detect Hα emission. We note that HCG 25b (an SBa) may be interacting with the small S0 galaxy HCG 25f, given an optical bridge seen between these two objects.

We find a disagreement between both sides of the rotation curve of HCG 25a, and this is usually taken as an indication that the galaxy has suffered interaction. However, we find no other signature for an ongoing merger or strong interaction event given that the velocity field of this galaxy is almost undisturbed. We tend to favour an early-stage-of-evolution scenario for this group although this conclusion is drawn from the kinematical observation of only one group member, HCG 25a, and from the inspection of the B and R images of HCG 25bf. More data are necessary to allow a better definition of the evolutionary stage of this triplet.

We observed three galaxies in group **HCG 44**, members a, c and d. HCG 44a displays little Hα emission in its centre, which is expected given its morphological type, Sa. No rotation curve could be derived. For HCG 44c, an SBc, we were able to derive the rotation curve. Just one indicator is flagged positive in this case. HCG 44d displays more indicators associated with an interaction event, however, given that this galaxy contains a strong bar, the interpretation of its velocity field is difficult and in addition no valuable rotation curve can be derived. This strong bar could have been induced by past strong tidal interactions although a secular origin could not be excluded. Gathering information for all galaxies, we do not find signatures of ongoing merger. However, Verdes-Montenegro et al. (2001) classified this system as a "Phase 3a" group, i. e., most of the HI gas has been stripped from the disk of the galaxies, which is an evidence of galaxy-galaxy interaction. These findings are in agreement with the giant HI tail recently discovered in this compact group by Serra et al. (2013); the authors suggest that this tail could be formed by a tidal effect (caused by the group) over HCG 44d. We may speculate that these results can support the origin of the strong bar of HCG 44d.

We observed three galaxies in **HCG 53**. Two of them show Hα emission (53a, an SBbc and 53c, an SBd). The third one (53b) is an S0 galaxy and does not have emission. HCG 53a does not have any signatures of interaction. HCG 53c has a few indicators flagged positive. It has a misalignment between the optical and kinematic major axis of the position angle. This signature can be a result of an interaction with its companion HCG 53b. In general, HCG 53 shows weak

Table 5. Interaction indicators based on Hα emission. In this table we have included all the galaxies for which we expect Hα emission following their morphological type. Description of the columns. Hα distribution: (A1) Lack of Hα emission which respect to what is expected taking into account the morphological type of the galaxy; (A2) Complex Hα structure; (A3) Tidal tails; (A4) Distorted spiral arms. Velocity Field: (B1) Highly disturbed velocity field; (B2) Gaseous versus stellar major-axis misalignment; (B3) Changing position angle along major axis. Rotation Curve (RC): (C1) Disagreement between both sides of the RC; (C2) Unexpected solid body behavior for the RC; (C3) Truncated rotation curve (shorter than R_{25})

Galaxy	Hα distribution				Velocity field			Rotation curve		
	A1	A2	A3	A4	B1	B2	B3	C1	C2	C3
HCG 1ab	+	...	+	...	+	−	...	+	+	+
HCG 14a	+	...	...	...	...	...	...	...	...	...
HCG 14c	+	...	...	...	...	...	...	...	...	...
HCG 25a	−	+	−	−	−	−	−	+	−	−
HCG 44a	+	...	...	...	...	...	...	...	...	...
HCG 44c	−	+	−	+	−	−	−	−	−	−
HCG 44d	−	+	−	+	+	...	...	...	...	...
HCG 53a	−	−	−	−	−	−	−	−	−	−
HCG 53c	−	−	−	−	−	+	−	−	+	+
HCG 57a	+	...	...	...	...	...	...	...	...	...
HCG 57b	+	...	...	...	...	...	...	...	...	...
HCG 57d	−	+	−	+	−	+	+	+	−	+
HCG 61c	+	...	...	...	...	...	...	...	...	...
HCG 69a	+	...	...	...	...	...	...	...	...	...
HCG 69b	+	...	...	...	...	...	...	...	...	...
HCG 93b	−	−	−	+	+	+	−	+	−	−
HCG 93c	+	...	...	...	...	...	...	...	...	...
VV 304a	−	+	−	+	−	+	+	+	−	+
VV 304b	−	+	−	+	+	+	+	+	−	+
NGC 7232	−	+	−	...	+	−	−	+	+	+
NGC 7232B	−	+	−	+	+	+	...	+	+	+
NGC 7233	−	+	−	+	+	...	...	−	+	+
Arp 314-1	−	+	+	+	+	+	+	+	−	+
Arp 314-2	−	+	+	+	+	...	+	+	+	−
Arp 314-3	−	+	+	+	+	+	...	−	+	−

signatures of galaxy-galaxy interactions, being, therefore, in an early stage of evolution..

We observed seven members of **HCG 57** and four of them are spiral galaxies, mainly galaxies a, b, d and h have types Sb, SBb, SBc and SBb respectively. We detect clear Hα emission only for member HCG 57d (a diffuse emission was detected in the central region of HCG 57a). HCG 57d has a regular velocity field, however, there is change in the kinematical position angle along the major axis. Both sides of its rotation curve do not match in the outer parts of this object and its velocity field seems to be connected with HCG 57a. A strong burst of star formation can be seen in a spiral arm. These interaction indicators suggest that this object is in an interaction process, and it is probably interacting with its companion galaxy HCG 57a. The lack of Hα emission in other members of this group can be associated with the detection limit of our observations, given that this system was observed with poor seeing conditions. This is further discussed in the next subsection.

We observed members a, c and d of **HCG 61** which have morphological types S0a, Sbc and S0, respectively. We have detected weak and non-extended Hα emission in the centres of these galaxies (in agreement with Vilchez et al. 1998, their Table 2, where the Hα emission for galaxies HCG 61a,c,d was classified as NE, i.e., nuclear emission). The morphological type of members a and c are in agreement with the lack of Hα emission. However, for HCG 61c, an Sbc galaxy, we would have expected a more pronounced and extended gas disk. This could indicate that interactions have taken place and have stripped the gas.

We observed four galaxies in **HCG 69**, members a, b, c and d, classified as Sc, SBb, S0 and SB0 respectively. We detected weak Hα emission in member HCG 69a, when we expected a strong signal, given its morphological type, and we did not detect emission in HCG 69b either, an SBb galaxy. This could be due to S/N problem of the data or, if true in nature, could be due to interactions which caused depletion of warm gas in the centres of the member galaxies.

We observed two galaxies of **VV 304** and both display clear signatures of galaxy-galaxy interactions. VV 304a has distorted spiral arms, but the velocity field is not strongly perturbed. However, we detect a disagreement between both sides of the rotation curve. In the case of VV 304b, seven out of ten interaction indicators are present. However, neither VV 304a nor VV 304b display optical tidal tails, which are clear signatures of strong galaxy encounters. This information suggests that the interaction process in VV 304 is still mild. However, given the apparent proximity of the members in VV 304, a merger event should occur.

The three observed galaxies in **LGG 455** were detected in Hα. NGC 7232 shows several signatures of interaction, like highly perturbed velocity field and disagreement between

both sides of the rotation curve. The same happens for NGC 7232B. NGC 7233 shows a perturbed velocity field, however, the rotation curve is symmetric, which is obviously a result of the azimuthal averaging.

The three galaxies observed in **Arp 314** were detected in Hα. The three members have most of the interaction indicators flagged positive. This fact shows that Arp 314 is in an advanced stage of evolution. This is consistent with the HI envelope that encloses this group.

4.1 Lack of warm gas in Hickson group galaxies?

Despite the fact that the compact groups studied in this paper are rather close to us, we detect five groups that contain Sb or later-type galaxies and which present weak or no Hα emission. These are groups HCG 1, HCG 14, HCG 57, HCG 61 and HCG 69.

For HCG 1ab, the Hα emission is mainly concentrated in a bridge between these two galaxies. In the case of HCG 61c, the Hα emission is faint and centrally concentrated (as also reported by Hα imaging from Vilchez et al. 1998). In the case of HCG 69a the emission is extended but quite faint. The worst cases are for HCG 14ac and 57abd, where we do not detect any Hα emission at all. On the other hand, we detect groups having galaxies (Sb or later) that display clear Hα emission, like HCG 25a, 44d, 53c, VV 304a, b and Arp 314 NED 01, 02 and 03. As mentioned, the complexity of the Hα emission and the lack of it in some galaxies can be used as an interaction indicator. However, we can not rule out the possibility that, at least in a few of the cases above, the lack of Hα emission is linked to the low S/N of the observations. In fact, this seems to be the case for HCG 57, given that Martinez et al. (2010) detected Hα emission in galaxies where we do not detect any signal. This idea is consistent with the observing conditions on which were obtained the Fabry-Perot data of HCG 57 (under poor seeing conditions).

Assuming the lack of Hα emission in some of the late type galaxies is real, we suggest that this can be related with interactions and with a late evolutionary stage of these compact groups. It is well known that interactions can remove some *neutral* gas of the galaxy disk and this gas can be ejected into the intergalactic medium, which has been shown by Verdes-Montenegro et al. (2001) to be at work in several compact groups. This scenario can result in a lack of ionized gas in the main body of the HCG galaxies. In fact, Plana et al. (1999) studied the HCG 92, also known as the Stefan Quintet, and they found that the spiral galaxies of this system do not show Hα emission or show little warm gas emission in their centres. Taking into account all information gathered in this paper, we argue this could indeed be the case for galaxies HCG 1ab and HCG 61c. These galaxies could have had their gaseous reservoirs removed, resulting in a quenching of their star formation. In the case of HCG 1, most of the Hα emission comes from a region located outside the main body of the galaxies. Note that groups HCG 1 and HCG 61 were found to have a normal HI content by Verdes-Montenegro et al. (2001), when the whole group was taken into account, which does not, however, conflict with the observations above.

Regarding the three other groups HCG 14, 57 and 69, we do not have enough data to conclude anything about their evolutionary stages. We note that these groups (as well as HCG 1, 25, 44 and 61) were observed with the OHP 1.93m-telescope, and not with the ESO 3.6m telescope where all the remaining data for compact group galaxies from this and our previous papers were obtained. One could argue that this may hint that the non-detection or weak detection is due to the lower S/N of the data. This idea is consistent with the study developed by Martinez et al. (2010), who found Hα emission in most of the galaxies belonging to HGC 57. Therefore the conclusion is that we really need more kinematic data for groups HCG 14, 57 and 69, which we plan to collect in the future to settle this question. However, taking into account that the GHASP (OHP) and CIGALE (ESO) instruments are similar and the setups almost identical, both detectors are similar and have the same size, the larger mirror size of the ESO telescope is almost compensated by the larger pixel size of the GHASP instrument. Thus, for a given extended source, observing time and atmospheric, telescope and filters transmissions, the SNR per pixel (but not by arcsec^2) should be roughly the same. Nevertheless, the main difference comes from the seeing conditions that dilute the Hα emission; the average seeing at OHP being worse than that at ESO (see Table 2), the SNR per pixel is on average higher for the ESO than for the OHP data. In addition, measurements of the narrow band filter transmission done after the OHP run, indicated that their transmission range between 70 and 80% (which are the expected values) except for four of them: the filters used to observe HCG 1, 14, 69 and 93 drop more or less drastically down to 40, 25, 55 and 25% respectively.

In this sample, we observe a total of 42 galaxies located in 12 compact groups. A total of 16/42 galaxies are E and S0/S0a. Three galaxies classified as S0a and two S0 galaxies display Hα emission. The other 11 E/S0/S0a galaxies do not present any Hα emission. The remaining 26/42 objects are non barred or barred spiral galaxies ranging from Sa to Im morphological types. We were able to derive velocity fields based on their Hα emission for 18/26 spiral galaxies, 5/16 E/S0/S0a galaxies and one Im galaxy. Among these 24 galaxies for which a velocity map was obtained, for 15 of them we could derive a rotation curve and among these 15 rotation curves only 2/15 show no signatures of interactions. In forthcoming papers, we will analyse these results in a broader context, including previously published results for other compacts groups.

5 ACKNOWLEDGEMENTS

We thank the anonymous referee for the useful comments that greatly improved this paper. We warmly thank Philippe Balard, Olivier Boissin, Benoît Epinat & Jean-Luc Gach for making the setup of the GHASP instrument on the 1.93m at OHP and Jacques Boulesteix & Jean-Luc Gach for the setup of the CIGALE instrument on the 3.6m at ESO. We also thank the OHP & ESO technical teams for support. S. T-F acknowledges the financial support of the project CONICYT PAI/ACADEMIA 7912010004. CB, MM and PA thank the PNCG (Program National Cosmologie et Galaxies) for partial funding of this project. CMdO, PA, CB and S.T-F would like to thank LabCosmos and USP-Cofecub for funding of collaboration visits in France, Brazil and

Chile. CMdO acknowledges funding from FAPESP (grant 2006/56213-9) and CNPq. HP thanks CNPq/CAPES for its financial support using the PROCAD project 552236/2011-0. S. T-F and D. O. acknowledges the financial support of the Dirección de Investigación of the Universidad de La Serena, through a "Concurso de Apoyo a Tesis 2013", under contract PT13145. This research has made use of the NASA/IPAC Extragalactic Database (NED) which is operated by the Jet Propulsion Laboratory, California Institute of Technology, under contract with the National Aeronautics and Space Administration. We also acknowledge the use of the HyperLeda database (http://leda.univ-lyon1.fr).

REFERENCES

Allam, S., Assendorp, R., Longo, G., Braun, M., & Richter, G. 1996, A&AS, 117, 39
Amram, P., Plana, H., Mendes de Oliveira, C., Balkowski, C., & Boulesteix, J. 2003, A&A, 402, 865
Arp, H. 1966, ApJS, 14, 1
Bitsakis, T., Charmandaris, V., Le Floc'h, E.; Díaz-Santos, T., Slater, S. K., Xilouris, E., Haynes, M. P. 2010, A&A, 517A, 75
Borthakur, S., Yun, M. S., Verdes-Montenegro, L. 2010, ApJ, 710, 385
Cluver, M. E. et al. 2013, ApJ, 765, 93
Daigle, O., Carignan, C., Hernandez, O., Chemin, L., & Amram, P. 2006, MNRAS, 368, 1016
Epinat, B., Amram, P., Marcelin, M., et al. 2008, MNRAS, 388, 500
Garcia, A. M. 1995, A&A, 297, 56
Garcia, A. M. 1993, A&AS, 100, 47
Gavazzi, G., Savorgnan, G., Fumagalli, M. 2011, A&A, 534A, 31
Gil de Paz, A., Boissier, S., Madore, B. F., et al. 2007, ApJS, 173, 185
Hickson, P. 1993, Atlas of Compact Groups of Galaxies (New York: Gordon and Breach Science Publishers)
Hickson, P., Mendes de Oliveira, C., Huchra, J. P., & Palumbo, G. G. 1992, ApJ, 399, 353
Hickson, P., Kindl, E., & Auman, J. R. 1989, ApJS, 7, 687
Hickson, P. 1982, ApJ, 255, 382
López-Sanjuan, C. et al. 2013, A&A, 553A, 78
Martínez M. A., Del Olmo A., Coziol R., Perea J., 2010, AJ, 139, 1199
Mendes de Oliveira, C., Hickson, P. 1994, ApJ, 427, 684
Mendes de Oliveira, C., Plana, H., Amram, P., Bolte, M., Boulesteix, J. 1998, ApJ, 507, 691
Mould, J. R. et al. 2000, ApJ, 529, 786
Nishiura, S., Shimada, M., Ohyama, Y., Murayama, T., Taniguchi, Y. 2000, AJ, 120, 1691
Plana, H., Amram, P., Mendes de Oliveira, C., Balkowski, C., & Boulesteix, J. 2003, AJ, 125, 1736
Plana, H., Mendes de Oliveira, C., Amram, P., Bolte, M., Balkowski, C., Boulesteix, J. 1999, ApJ, 516L, 69
Renaud, F., Appleton, P. N., Xu, C. K. 2010, ApJ, 724, 80
Serra, P. et al. 2013, MNRAS, 428, 370
Torres-Flores, S., Mendes de Oliveira, C., de Mello, D. F., et al. 2009, A&A, 507, 723
Torres-Flores, S., Mendes de Oliveira, C., Amram, P., Plana, H., Epinat, B., Carignan, C., Balkowski, C. 2010, A&A, 521A, 59
Torres-Flores, S., Mendes de Oliveira, C., Plana, H., Amram, P., Epinat, B. 2013, MNRAS, 432, 3085
Verdes-Montenegro, L., Yun, M. S., Williams, B. A., et al. 2001, A&A, 377, 812
Verdes-Montenegro, L., Del Olmo, A., Yun, M. S., Perea, J., 2005, A&A, 430, 443
Vilchez, J. M., & Iglesias-Páramo, J. 1998, ApJS, 117, 1
Vogt, F. P. A., Dopita, M. A., Kewley, L. J. 2013, ApJ, 768, 151
Vorontsov-Velyaminov, B. A. 1959, Atlas and Catalog of Interacting Galaxies, Part 1 (Moscow: Sternberg Inst., Moscow State Univ.)

APPENDIX A: DIGITAL SKY SURVEY OPTICAL IMAGES, Hα MONOCHROMATIC MAPS, VELOCITY FIELDS, VELOCITY DISPERSION MAPS AND ROTATION CURVES FOR THE GALAXIES OF THIS SAMPLE.

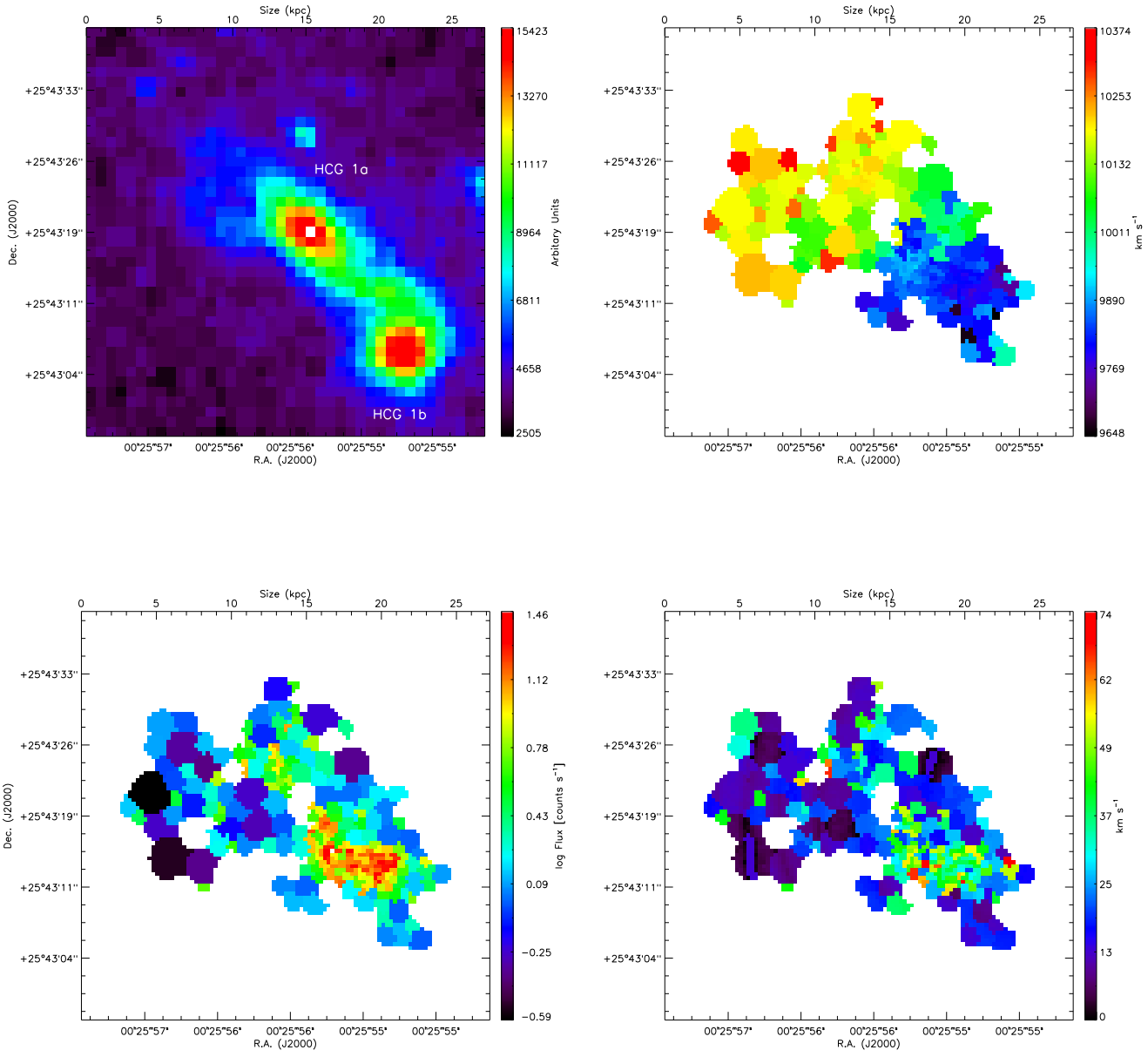

Figure A1. Maps for HCG 1ab. Top left: B band image from DSS. Top right: velocity field. Bottom left: monochromatic image. Bottom right: velocity dispersion map.

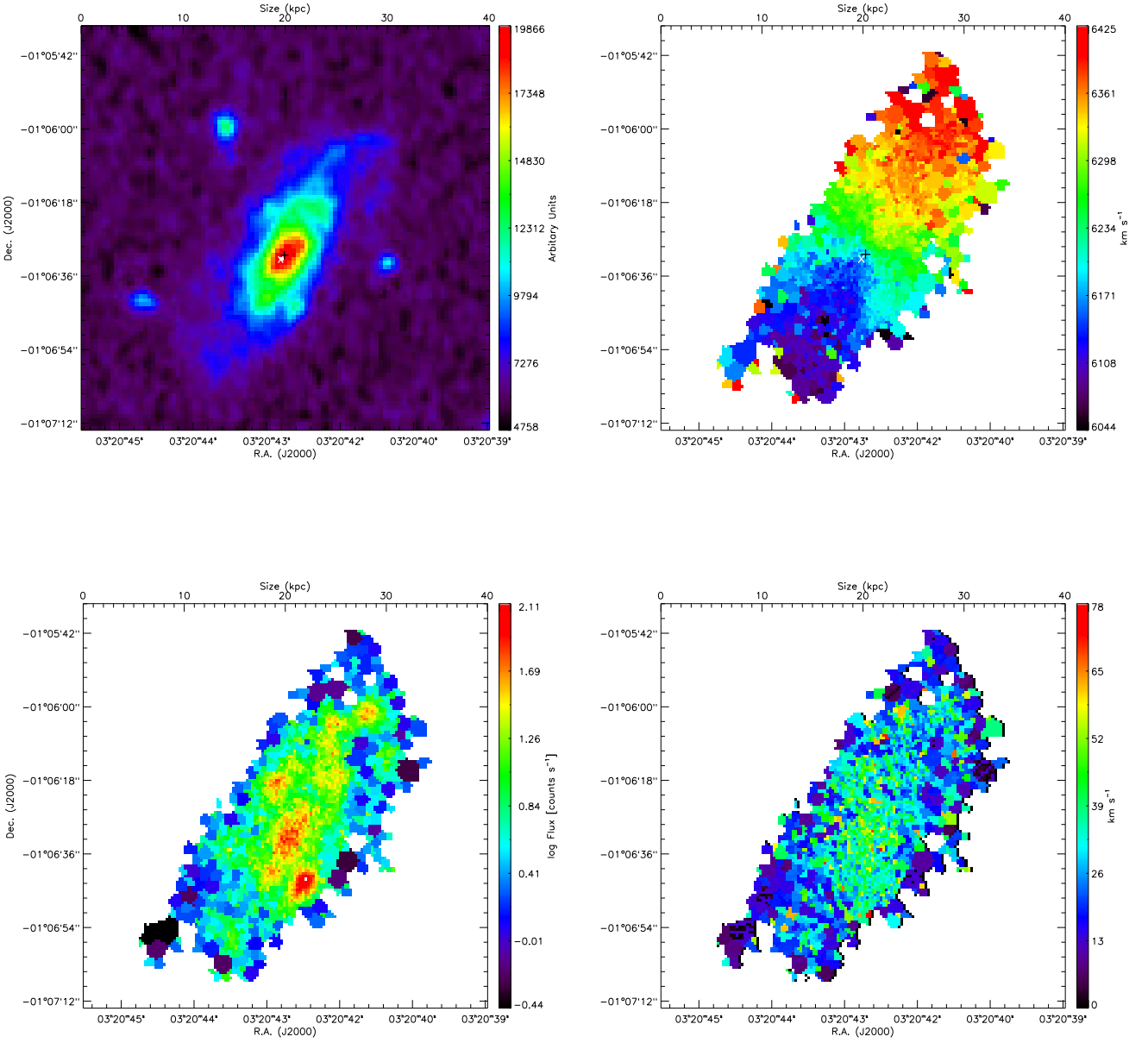

Figure A2. Maps for HCG 25a. Top left: B band image from DSS. Top right: velocity field. Bottom left: monochromatic image. Bottom right: velocity dispersion map. The white "x" sign indicate the position of the photometric centre while the black "+" sign indicate the position of the kinematic centre.

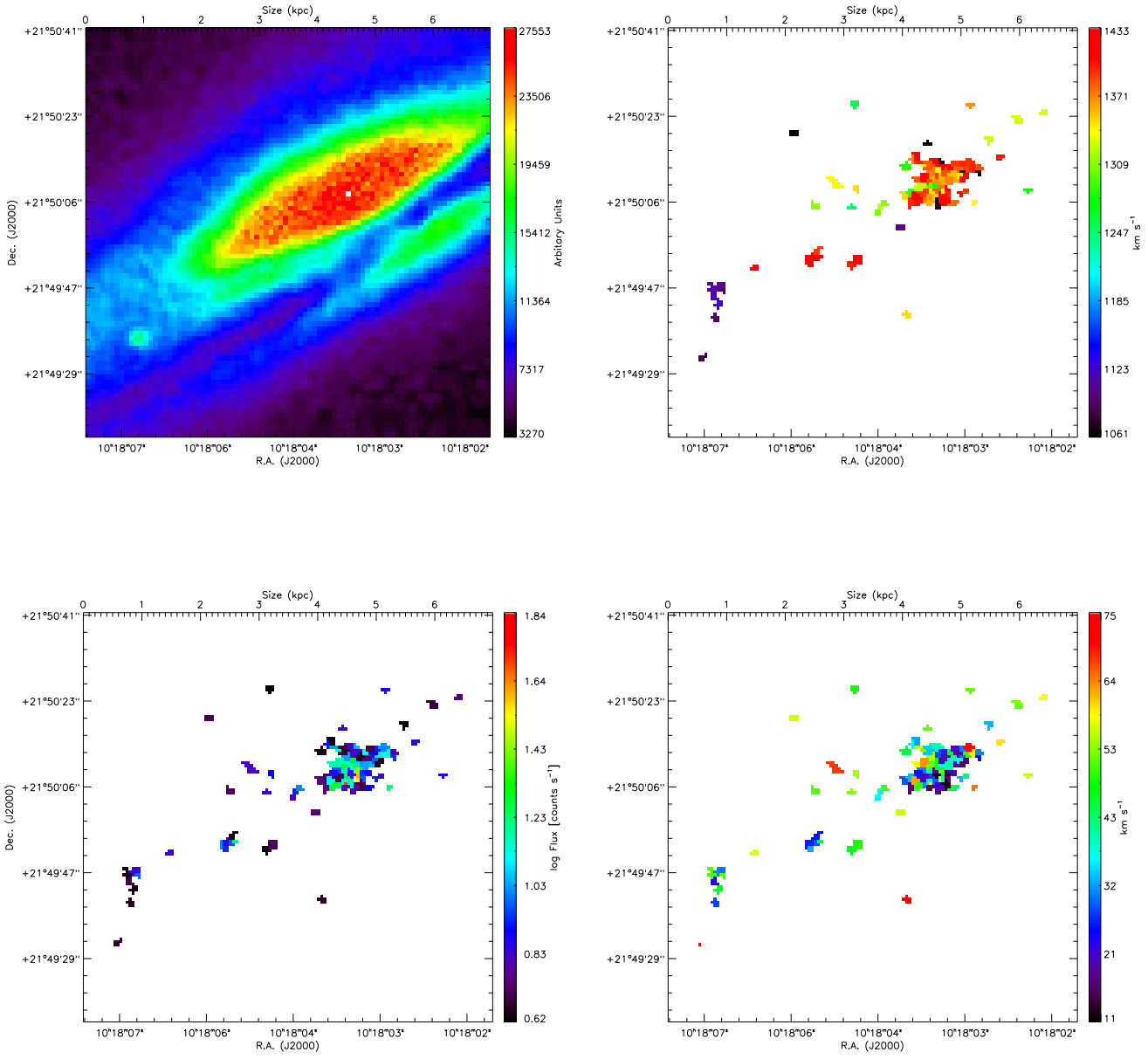

Figure A3. Maps for HCG 44a. Top left: B band image from DSS. Top right: velocity field. Bottom left: monochromatic image. Bottom right: velocity dispersion map.

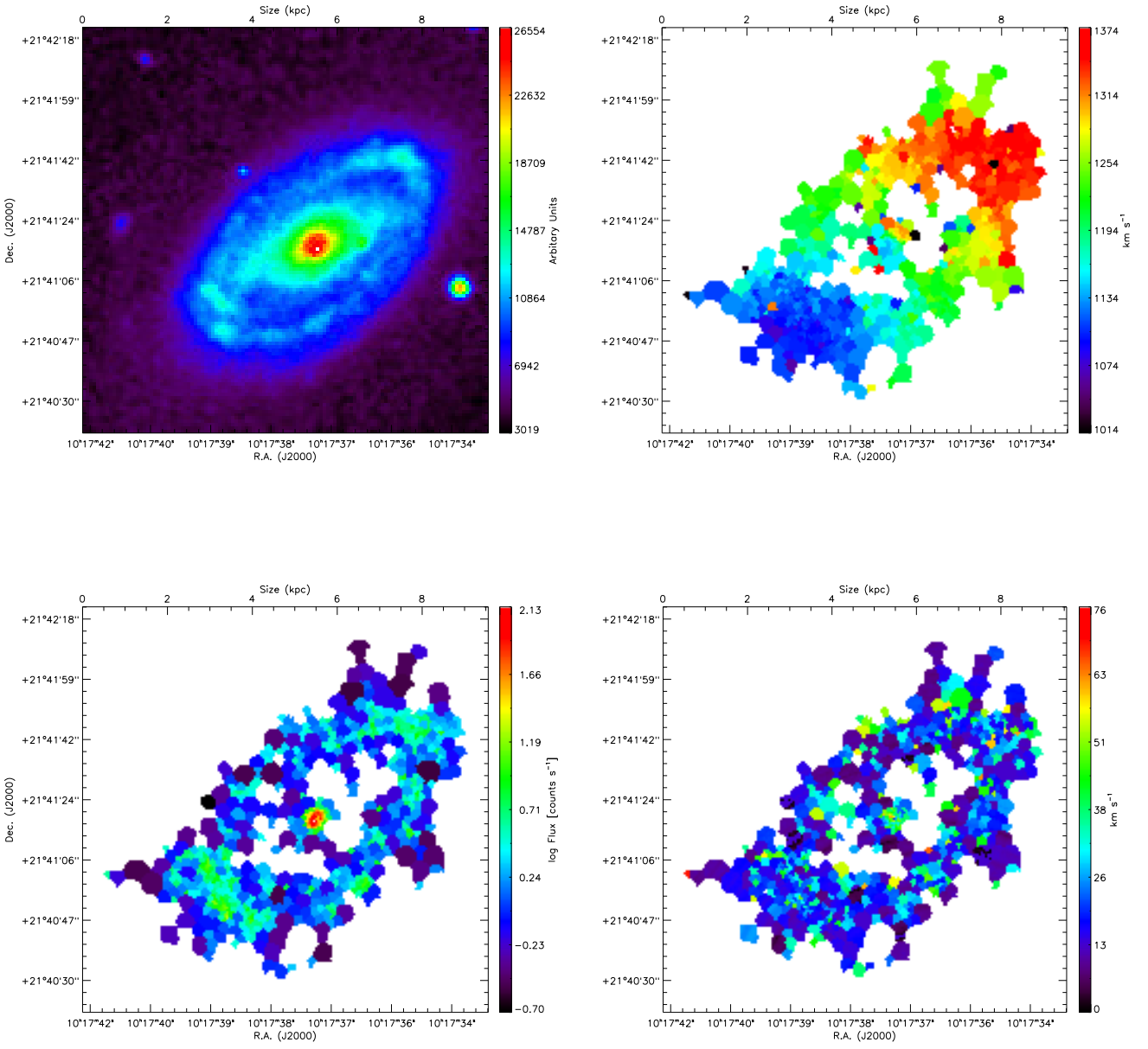

Figure A4. Maps for HCG 44c. Top left: B band image from DSS. Top right: velocity field. Bottom left: monochromatic image. Bottom right: velocity dispersion map.

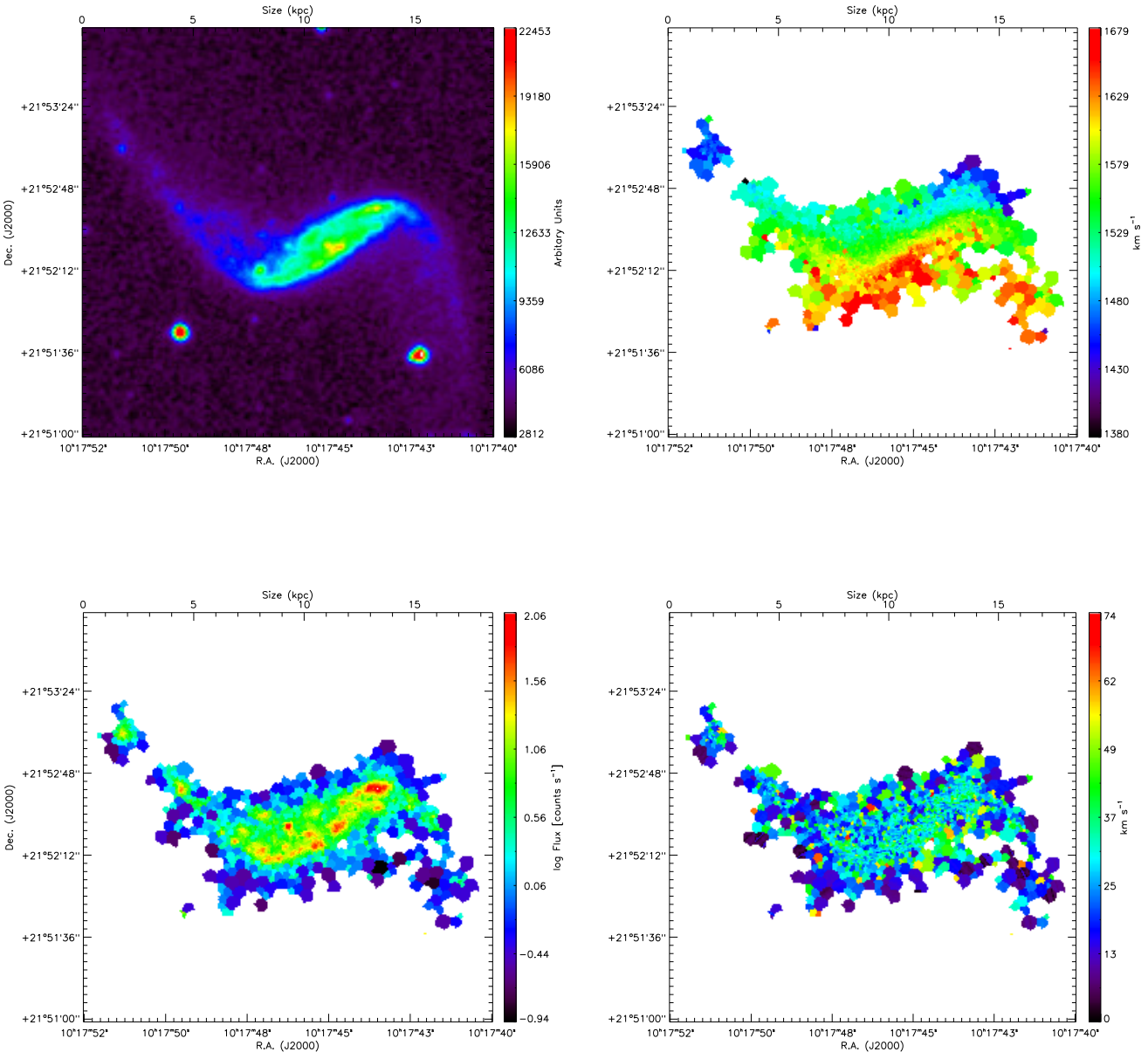

Figure A5. Maps for HCG 44d. Top left: B band image from DSS. Top right: velocity field. Bottom left: monochromatic image. Bottom right: velocity dispersion map.

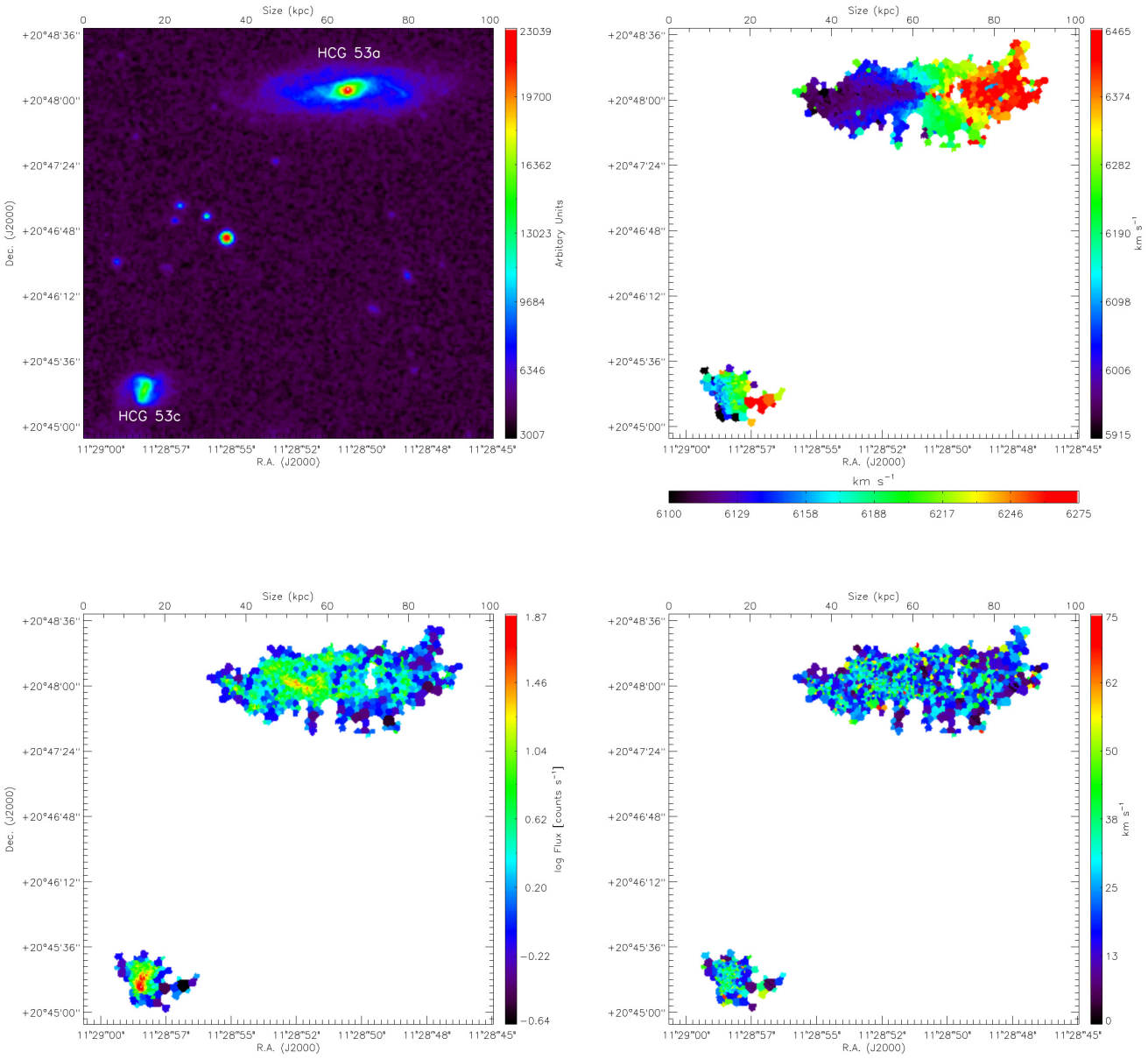

Figure A6. Maps for HCG 53ac. Top left: B band image from DSS. Top right: velocity field, where the bottom colour bar corresponds to HCG 53c. Bottom left: monochromatic image. Bottom right: velocity dispersion map.

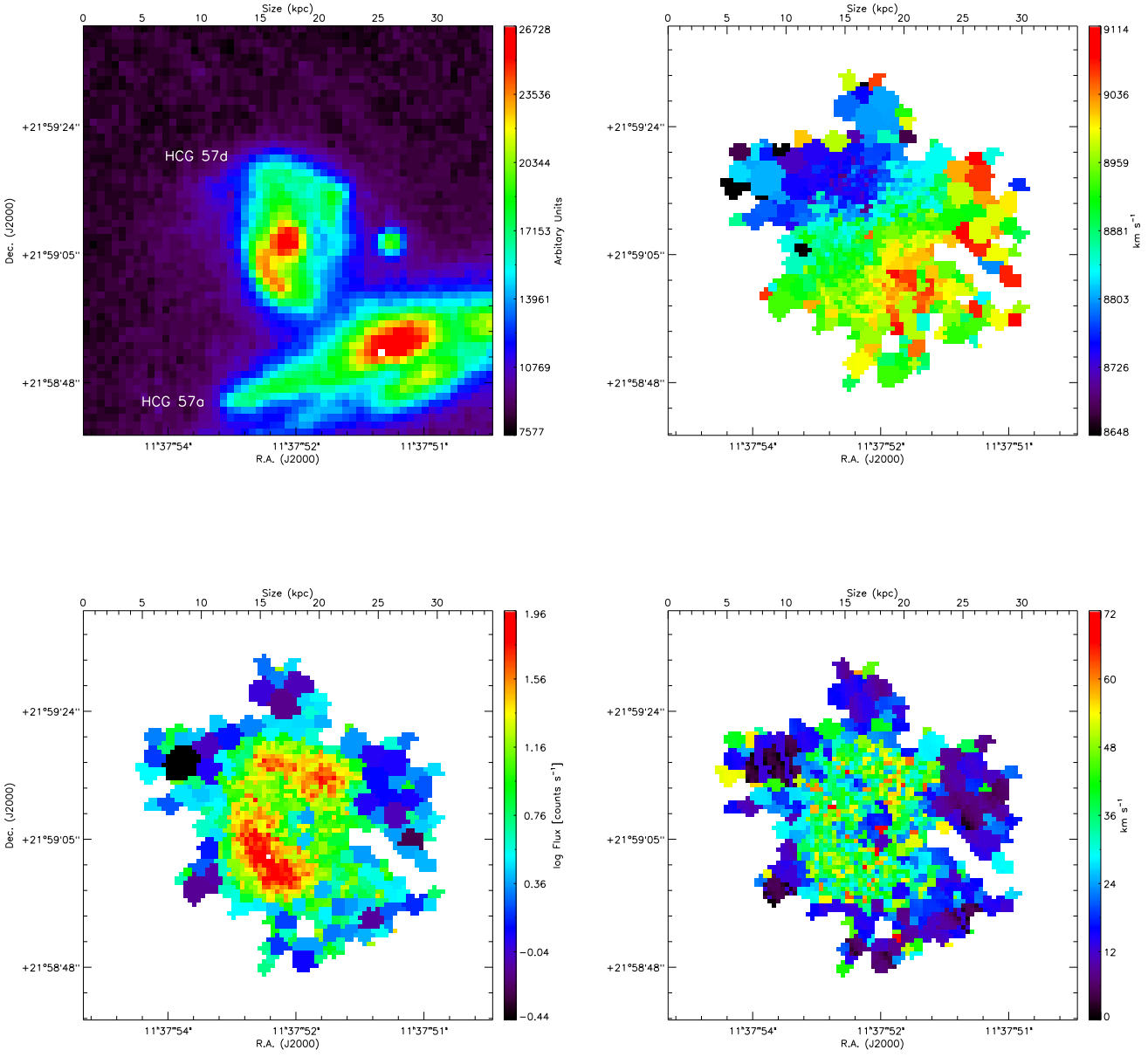

Figure A7. Maps for HCG 57ad. Top left: B band image from DSS. Top right: velocity field. Bottom left: monochromatic image. Bottom right: velocity dispersion map.

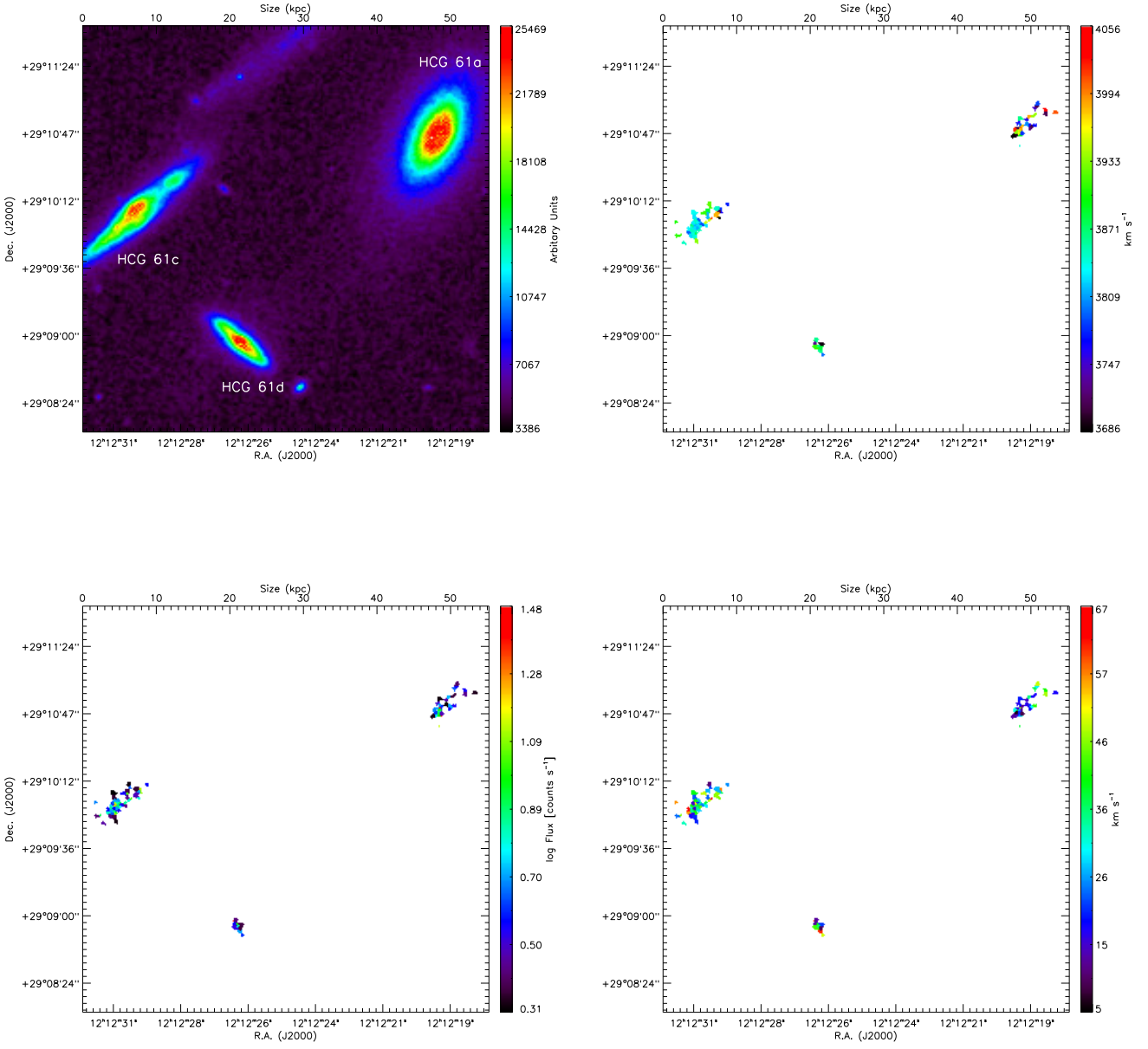

Figure A8. Maps for HCG 61acd. Top left: B band image from DSS. Top right: velocity field. Bottom left: monochromatic image. Bottom right: velocity dispersion map.

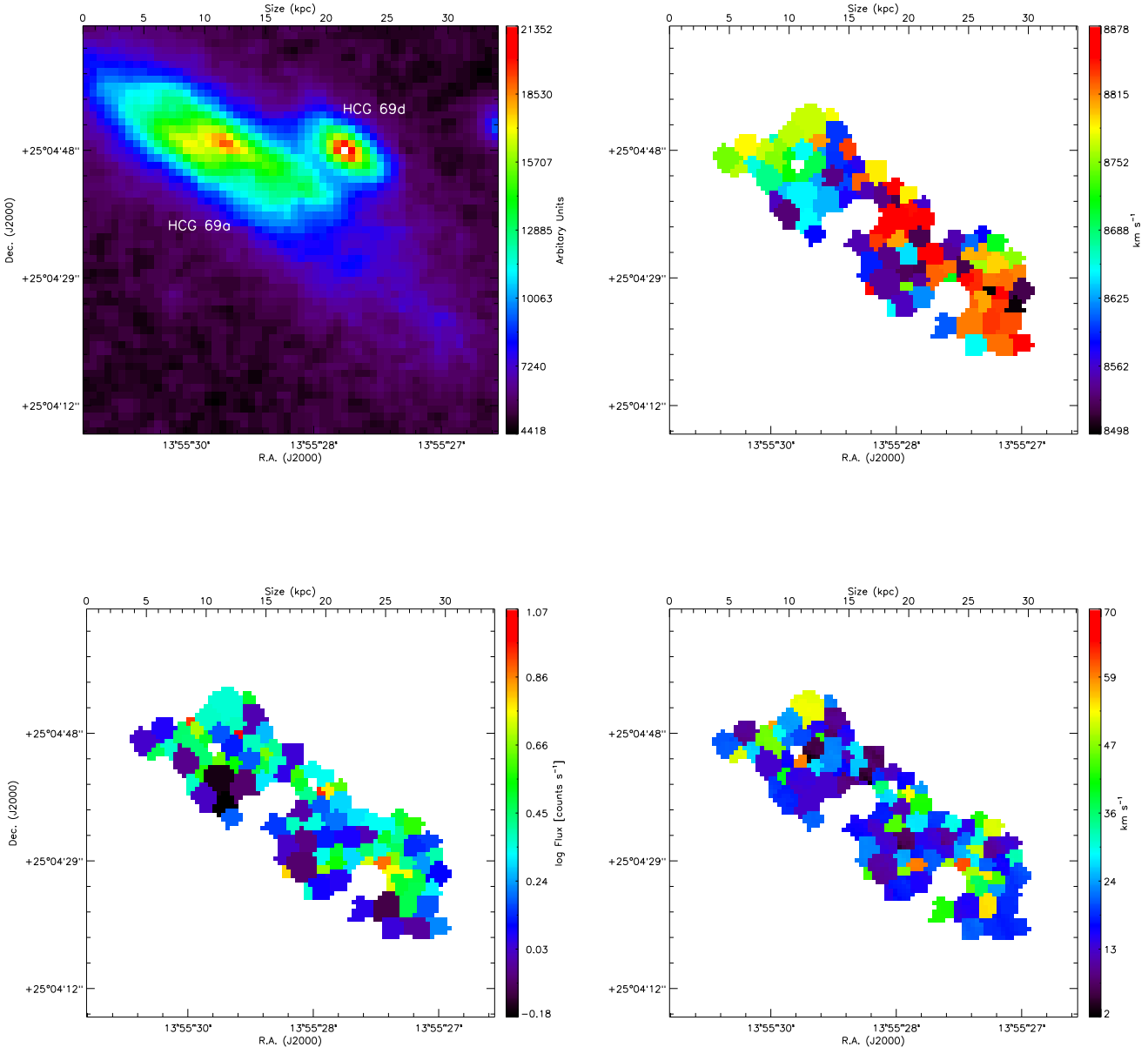

Figure A9. Maps for HCG 69ad. Top left: B band image from DSS. Top right: velocity field. Bottom left: monochromatic image. Bottom right: velocity dispersion map.

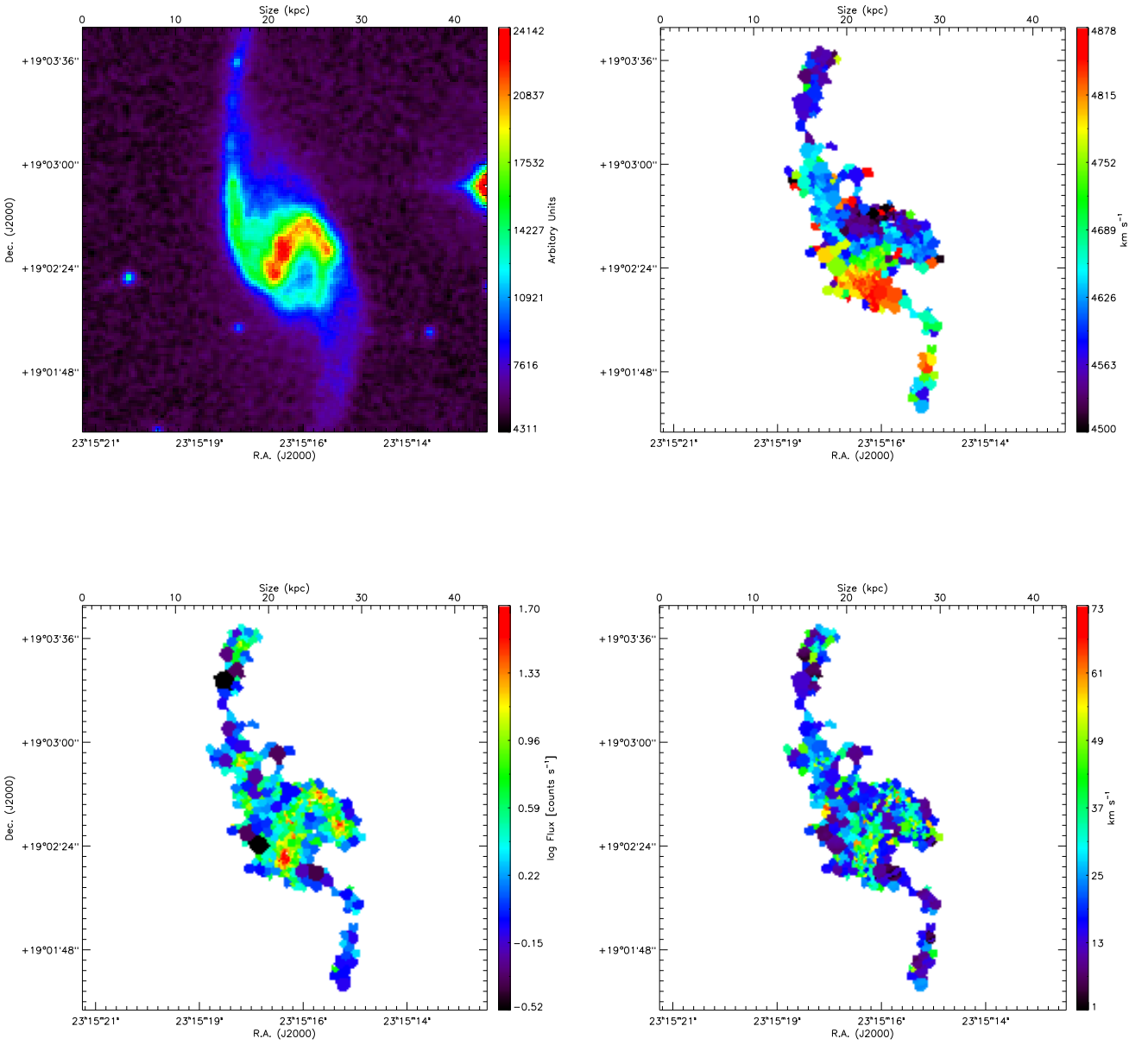

Figure A10. Maps for HCG 93b. Top left: B band image from DSS. Top right: velocity field. Bottom left: monochromatic image. Bottom right: velocity dispersion map.

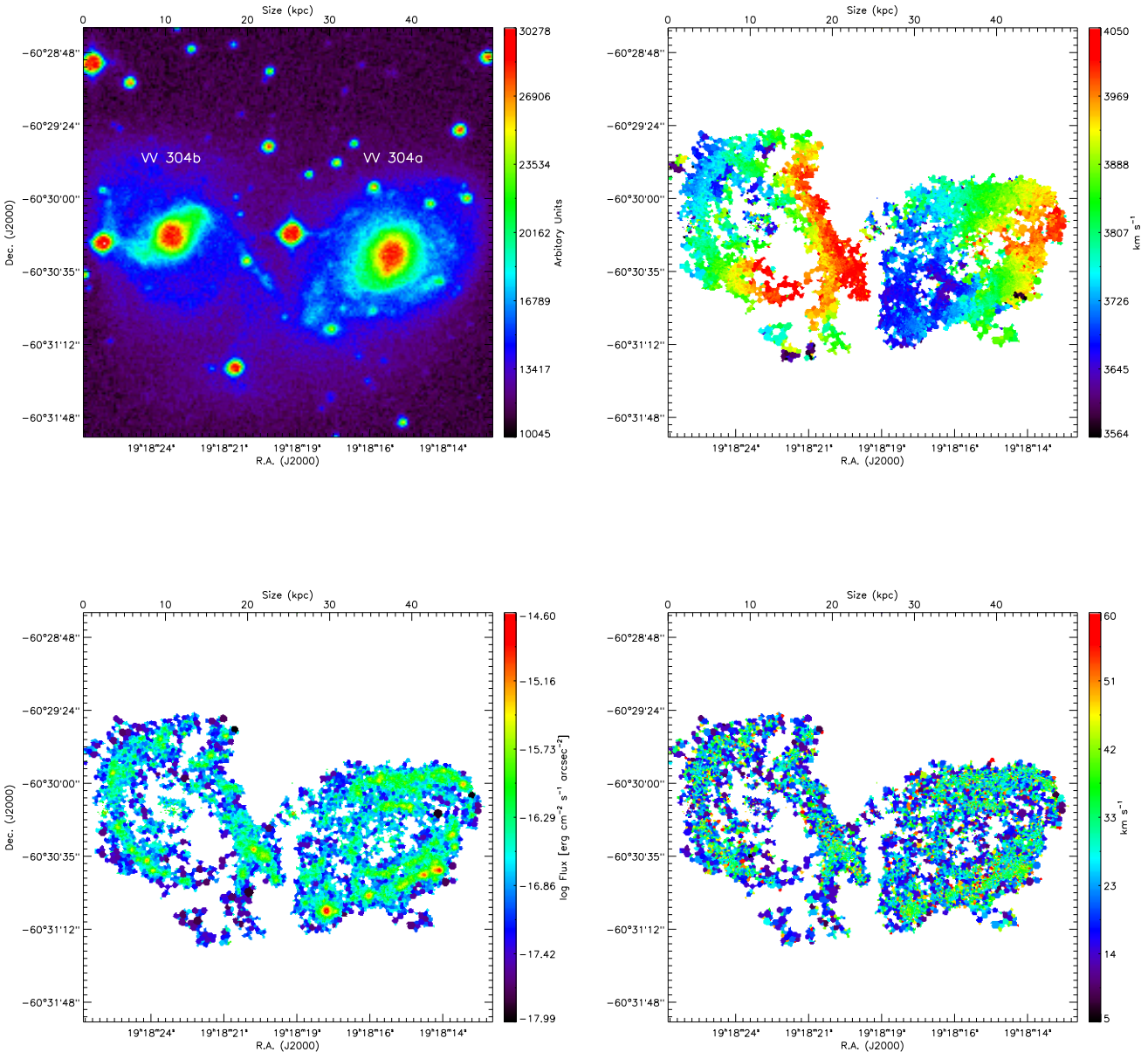

Figure A11. Maps for VV 304ab. Top left: B band image from DSS. Top right: velocity field. Bottom left: monochromatic image. Bottom right: velocity dispersion map.

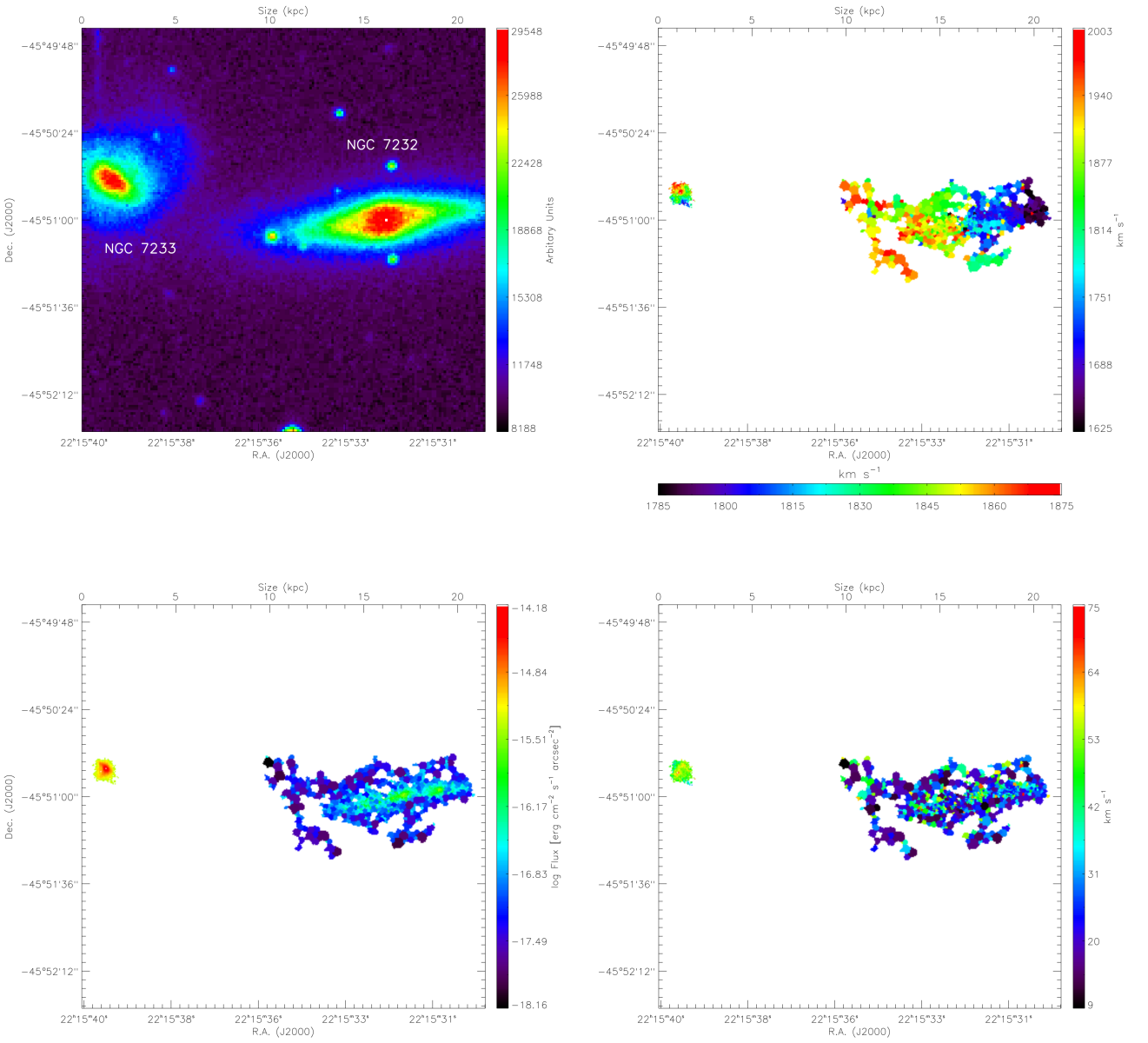

Figure A12. Maps for LGG 455. Top left: B band image from DSS. Top right: velocity field, where the bottom colour bar corresponds to NGC 7233. Bottom left: monochromatic image. Bottom right: velocity dispersion map.

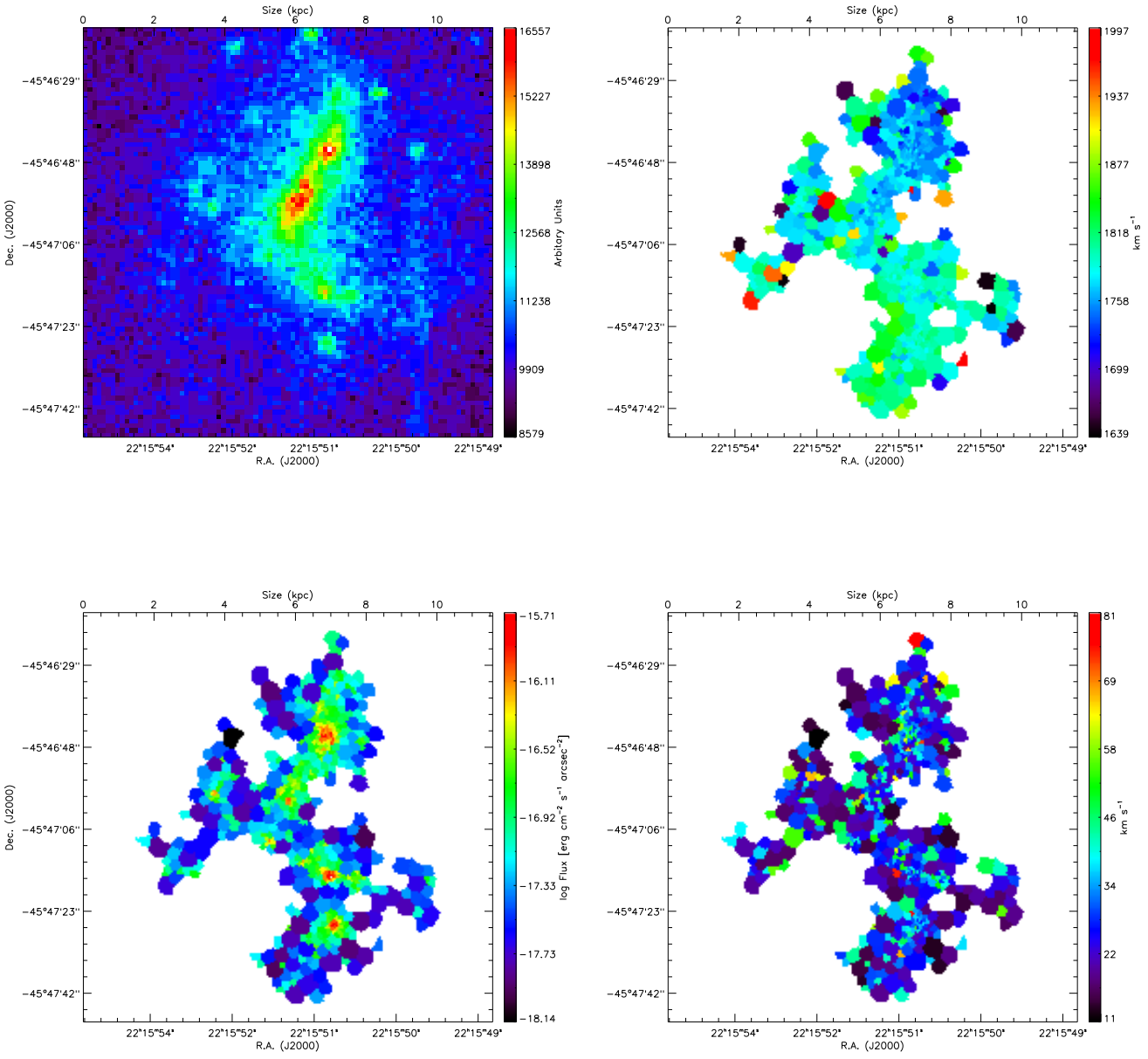

Figure A13. Maps for LGG 455 (member NGC 7232B). Top left: B band image from DSS. Top right: velocity field. Bottom left: monochromatic image. Bottom right: velocity dispersion map.

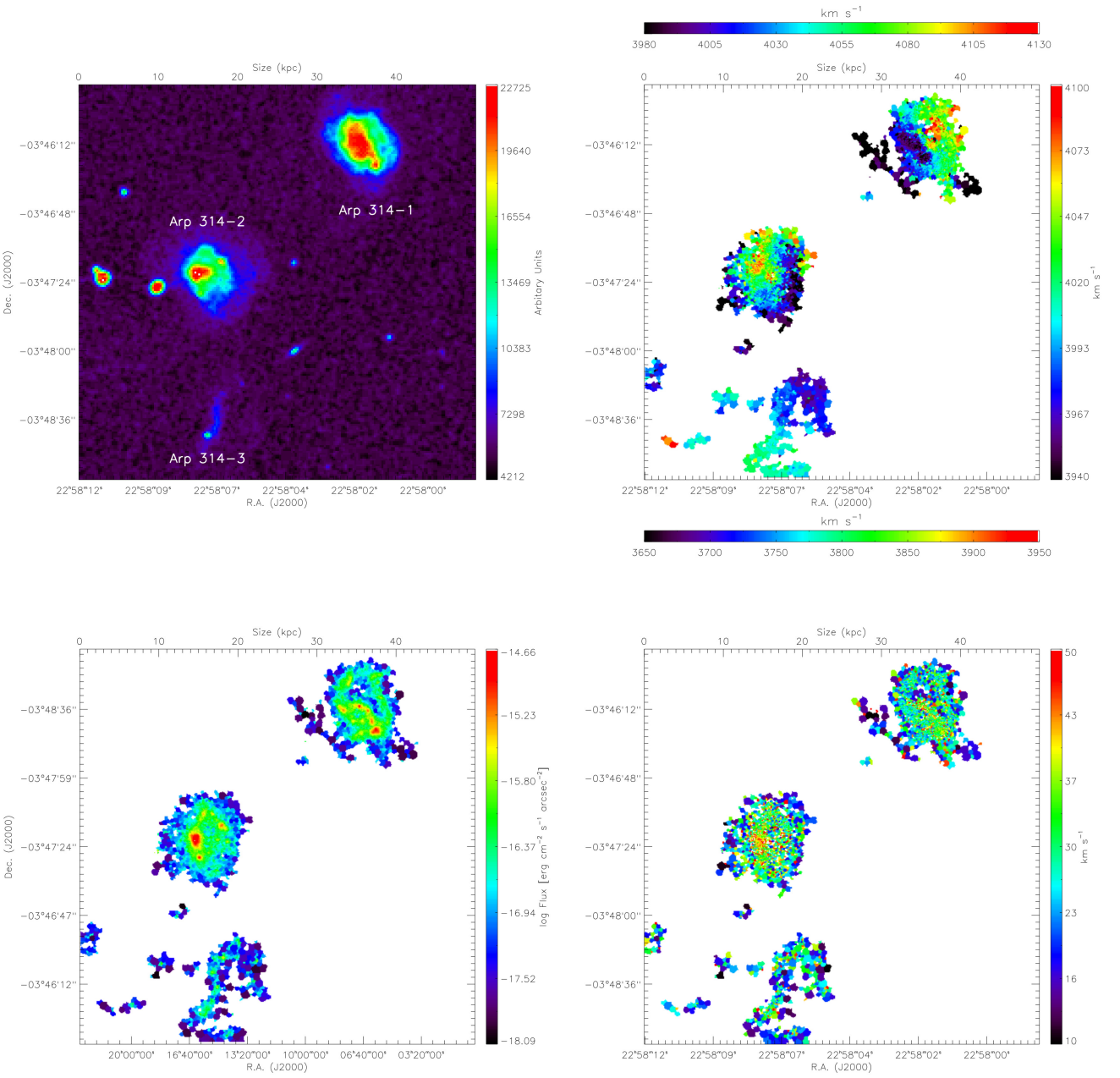

Figure A14. Maps for Arp 314. Top left: B band image from DSS. Top right: velocity field, where the upper, right and bottom colour bars correspond to Arp 314-1, Arp 314-2 and Arp 314-3, respectively. Bottom left: monochromatic image. Bottom right: velocity dispersion map.

APPENDIX B: ROTATION CURVES.

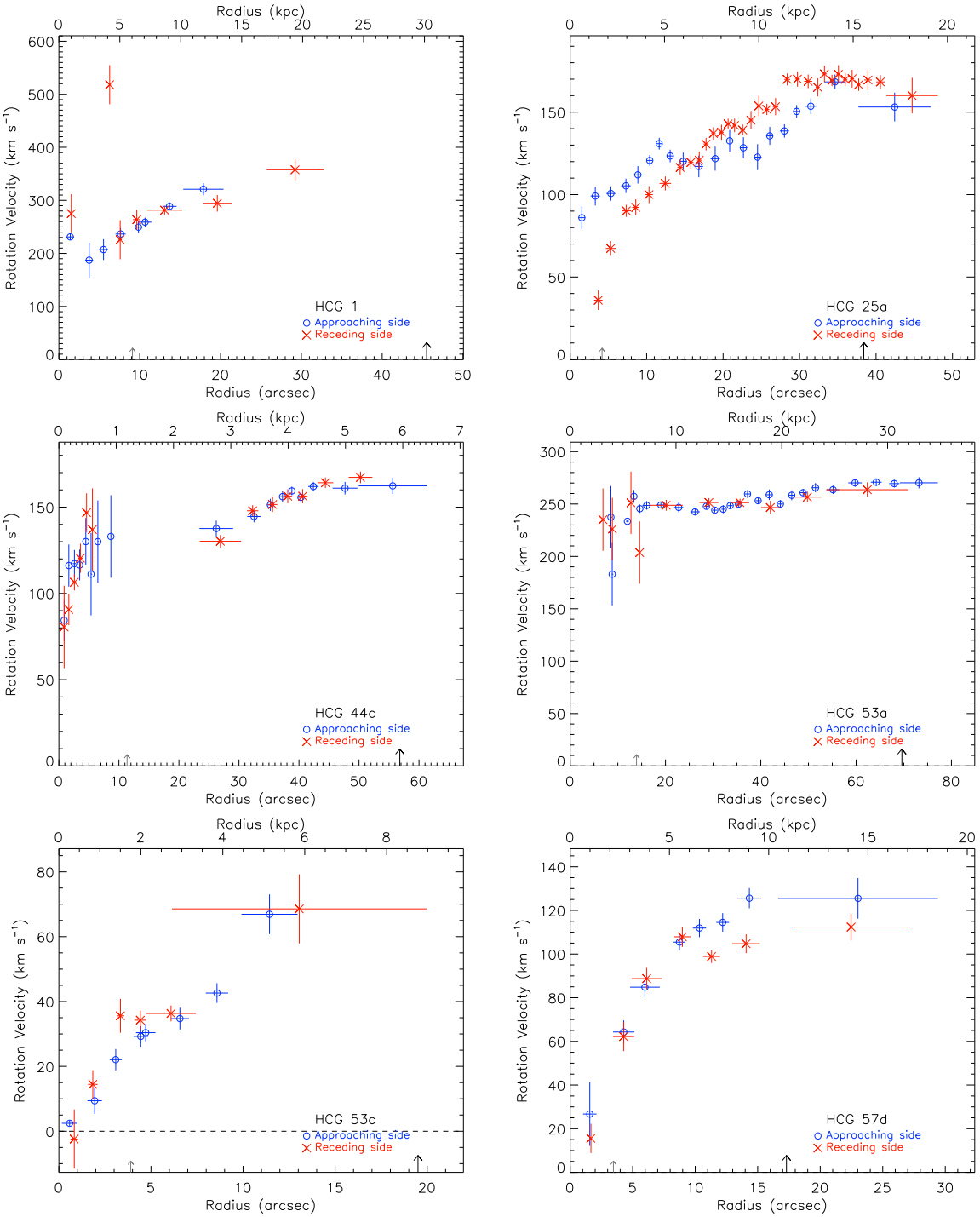

Figure B1. Rotation curves in this sample. The PA and inclination were determinated automatically from the model. The centre was fixed (mophological centre). The black vertical arrow in the x-axis represents the radius R25 while the smaller grey arrow in the x-axis represents the transition radius that is defined by the first ring that contains more than 25 uncorrelated bins in the velocity field (see Epinat et al. 2008a). The horizontal error bars represent the width of the rings containing 25 bins except in the inner region (defined by the grey arrow). The vertical bars are the 1σ uncertainty in the rotation velocity determination within each ring.

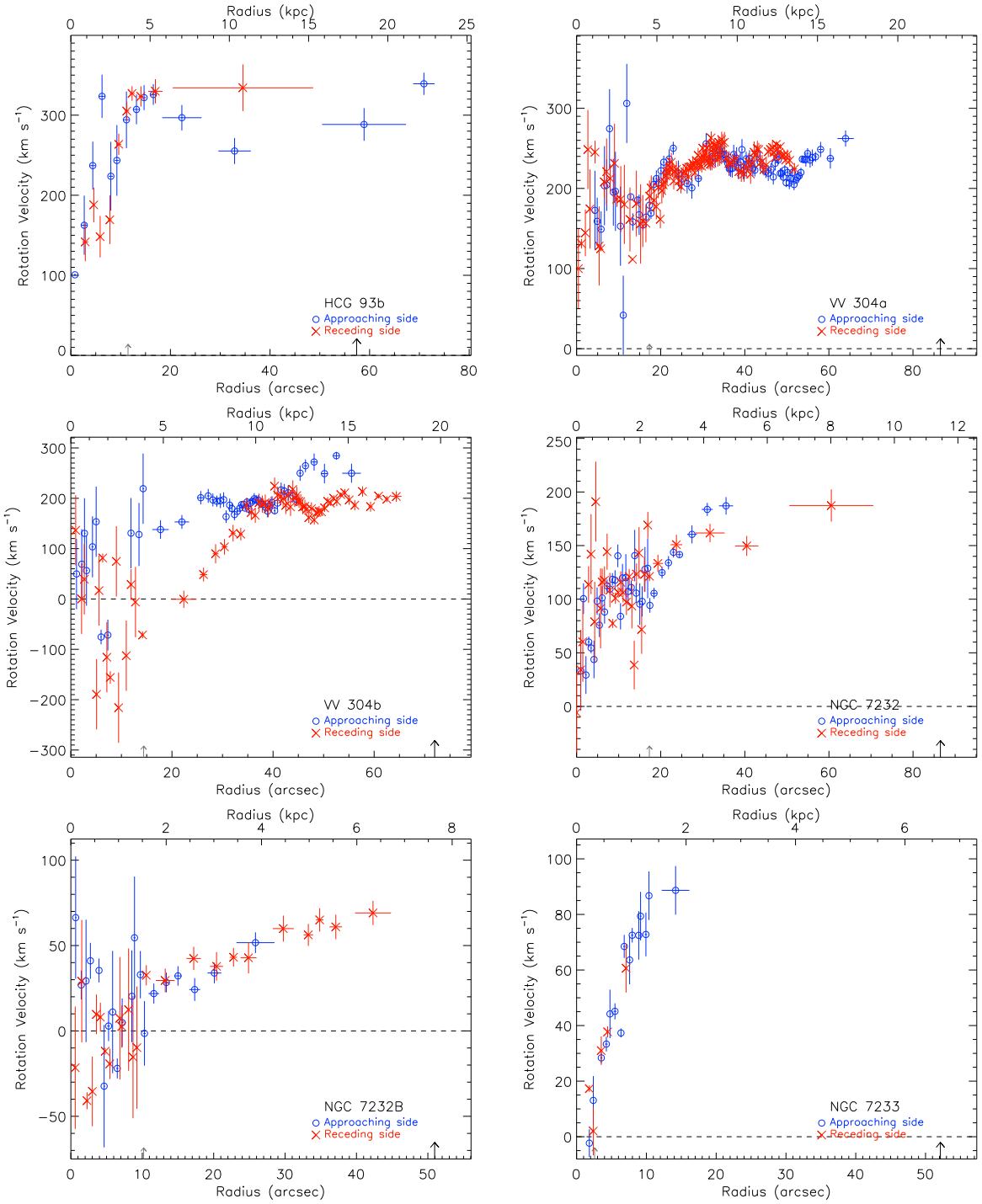

Figure B1. Continued

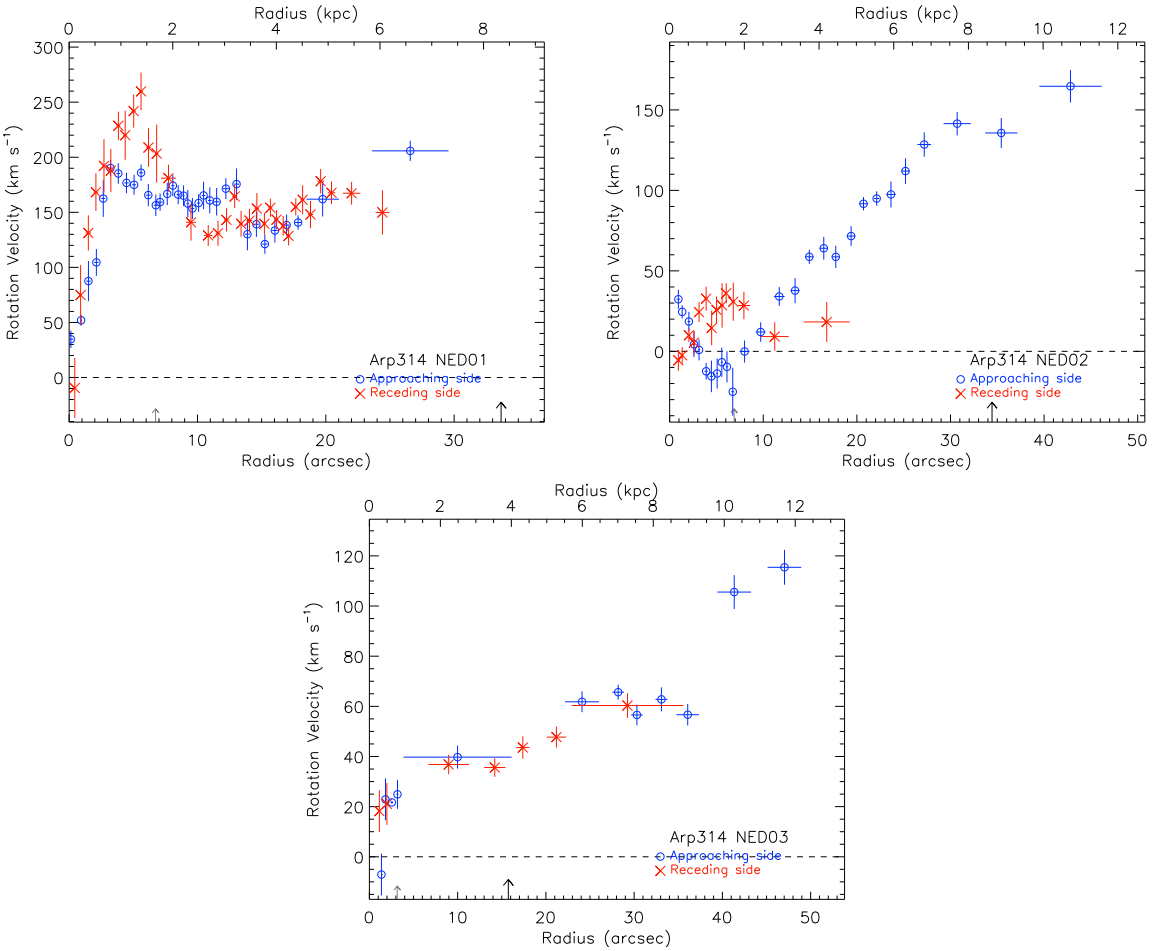

Figure B1. Continued